J. Fluid Mech. (1993), *vol.* 250, *pp.* 1–42

A direct numerical simulation of laminar and turbulent flow over riblet-mounted surfaces

By DOUGLAS C. CHU AND GEORGE EM KARNIADAKIS
Princeton University, Department of Mechanical and Aerospace Engineering, Program in Applied and Computational Mathematics, Princeton, NJ 08544, USA

(Received 24 December 1991 and in revised form 8 October 1992)

The flow in a channel with its lower wall mounted with streamwise riblets is simulated using a highly efficient spectral element–Fourier method. The range of Reynolds numbers investigated is 500 to 3500, which corresponds to laminar, transitional, and turbulent flow states. A complete study is presented for V-groove riblets; the effect of rounded riblets is also investigated. Our results suggest that in the laminar regime there is no drag reduction, while in the transitional and turbulent regimes drag reduction exists (approximately 6% at Reynolds number 3500) for the riblet-mounted wall in comparison with the smooth wall of the channel. For the first time, we present detailed turbulent statistics (turbulence intensities, Reynolds shear stresses, skewness and flatness) as well as a temporal analysis using a numerical analog of the VITA technique. The flow structure over the riblet-mounted wall is also analysed in some detail and compared with the corresponding flow over the smooth wall in an attempt to identify the physical mechanisms that cause drag reduction. The accuracy of the computation is established by comparing flow quantities corresponding to the smooth wall with previous direct numerical simulation results as well as with experimental results; on the riblet-mounted wall comparison is made with available experimental results. The agreement is very good for both cases. The current computation is the first *direct* numerical simulation of turbulence in a complex geometry domain.

1. Introduction

In recent years, turbulent boundary-layer drag reduction has become an important area of fluid dynamics research. Rising fuel costs in the 1970s greatly emphasized the usefulness and necessity of developing efficient viscous drag reduction methods. Many classes of transport and other important applications stand to reap great rewards from the successful application of viscous drag reduction techniques. Some examples are: commercial transport aircraft, high-speed aircraft and missiles, surface ships that operate at low Froude number, submarines and other underwater bodies, and long distance pipelines.

In the search for viscous drag reduction, many different techniques have been developed and investigated (Bushnell & Hefner 1990; Coustols & Savill 1992; Falco, Klewicki & Pan 1989; Kline & Robinson 1989; Smith & Metzler 1983; Tsinober 1989; Walker *et al.* 1987). Some examples that may be categorized as active techniques are: boundary-layer suction or wall heating to delay transition, modification of the fluid viscosity by injection of polymers or changing the fluid temperature, the use of compliant walls, and active wave control of boundary-layer transition. Other examples that can be considered passive techniques are natural laminar flow control (pressure-gradient/wall shaping), and modification of outer flow structures with devices such as 'large eddy breakup devices' (LEBUs). One of the more interesting techniques is the drag reduction method involving the use of 'riblets'. Riblets are micro-grooves on the bounding surface that are aligned with the mean flow direction; this method is particularly attractive due to its completely passive nature. It seems that the concept of using a grooved surface to reduce drag may have already been implemented in nature: the skin of some species of fast-swimming sharks have three-dimensional riblets on them as has been reported by Bechert, Bartenwerfer & Hoppe (1986) and Bushnell & Moore (1991).

Riblets have been thoroughly investigated in the work of Bacher & Smith (1985), Bechert & Bartenwerfer (1989), Choi (1989), Coustols & Cousteix (1989), Djenidi *et al.* (1986), Gaudet (1987), Liu *et al.* (1989), Robinson (1989), Roon & Blackwelder (1989), Squire & Savill (1986), Tani (1988), Vukoslavčević, Wallace & Balint (1987), and Walsh (1990*a*) in recent years. A considerable amount of experimental data has been collected regarding the flow over various shapes, sizes, and spacings of riblets in the turbulent regime. Riblets were successfully employed in the 1987 America's Cup competition, and have already been tested at flight conditions (Robert 1992; Robinson 1988; Walsh 1990*b*). It has been found that drag reduction on the order of 8% can be achieved for flow over a flat plate mounted with riblets, if the proper spacings and heights are used (Walsh 1990*b*). Walsh and co-workers at NASA Langley have performed extensive experiments on the effects of riblet shapes and dimensions, and conclude that the optimal shape may be that of the 'shark-scale riblet' (see also Bechert & Bartenwerfer 1989). This riblet, however, is difficult to machine; the symmetric triangular riblet is therefore used in most experiments as the optimal drag-reducing riblet. This is the riblet shape we focus on in this study. Vukoslavčević *et al.* (1987) have made careful, precise measurements of the velocity field and turbulence statistics over triangular riblets; our results in §4 show good agreement with these particular experimental results, among others.

Although there has been a tremendous effort in the area of riblet research in recent years, most of the results obtained to date are experimental. There is a significant dearth of relevant numerical data (i.e. accurate turbulent flow riblet computations) to complement and enhance the experimental findings. There have been some computations performed involving flow over riblets in the laminar regime (Djenidi *et al.* 1986; Choi, Moin & Kim 1991), and numerical simulations involving boundary-layer equations, but most of these assume that the flow inside the riblet valleys can be modelled as a steady laminar flow; we show in §4 that this is incorrect, since the flow is unsteady in the high Reynolds number regimes. Some turbulent flow computations have been performed by Khan (1986) and Launder & Savill (1988), but these simulations use parabolized equations (thus neglecting strong streamwise variations) and employ various turbulence models. Direct numerical simulations providing detailed information about the inner turbulent boundary-layer structure should prove useful in assessing the validity of various turbulence models for smooth/rough wall flows, and in helping to construct new turbulence models.

As yet, no clear quantitative explanations of the turbulent drag mechanism(s) of riblets have been confirmed. More information about the structure of the flow near and in the riblet valleys is needed; this can be reliably provided by careful numerical simulations. This need for a more complete investigation is what motivated this current research project; a complete numerical study of the flow over riblets has been undertaken. The three-dimensional incompressible Navier–Stokes equations are solved via direct numerical simulation (DNS) using a spectral element–Fourier method to investigate the laminar and turbulent regimes of the flow over riblet-mounted surfaces. Since DNS is employed without any turbulence models, only low Reynolds number turbulent flows are investigated in the present work. It is assumed that insight into the drag reduction mechanisms of riblets will still be provided at these Reynolds numbers, and that our results at low Reynolds numbers will prove useful for future investigations at higher *Re* in the turbulent regime. Experimental evidence by Walsh (1990*a*) suggests that at higher speeds the relative drag reduction is even higher. The results in §4 include, to the best of our knowledge, the first turbulence statistics reported in a three-dimensional, complex-geometry, Navier–Stokes direct numerical simulation.

Section 2 will briefly outline the basic methodology and numerical formulation of the spectral element–Fourier method. It will also discuss convergence properties and provide a brief summary of the computational implementation and code performance. Section 3 discusses the computational domain, mesh resolution, and numerical procedures involving the transition to turbulence. Most of the results of this study are documented in §4: laminar flow results, turbulent mean flow properties, turbulence statistics, flow structure and physics, drag reduction, and comparisons in the laminar regime with rounded riblets are all included. We then conclude with a brief summary and discussion.

2. Formulation and methodology

2.1. *Governing equations*

We consider the flow of incompressible Newtonian fluids governed by the Navier–Stokes equations of motion,

$$\frac{\mathrm{D}\boldsymbol{v}}{\mathrm{D}t} = -\frac{\nabla p}{\rho} + Re^{-1}\nabla^2\boldsymbol{v} \quad \text{in} \quad \Omega, \tag{1a}$$

$$\nabla\cdot\boldsymbol{v} = 0 \quad \text{in} \quad \Omega, \tag{1b}$$

where $\boldsymbol{v}(\boldsymbol{x},t)$ is the velocity field, p is the static pressure, ρ is the density, $Re = [W]H/\nu$ is the Reynolds number, $[W]$ is the bulk streamwise velocity, H is a characteristic length, and ν is the kinematic viscosity (see §3.1 for more specific definitions of $[W]$ and H). Here D denotes the total derivative. We note now that our coordinate system is different from the standard system used in channel flow simulations: z is the streamwise direction, x is the spanwise direction, and y is the normal direction.

We consider only flows for which the mean varies arbitrarily in the (x,y)-plane and remains unchanged along the third (z) direction. This assumption of z-homogeneity simplifies the formulation of the governing equations, since only the instantaneous flow needs to be represented along all three directions, whereas the geometry remains effectively two-dimensional. We employ spectral element discretizations in (x,y)-planes and spectral Fourier expansions along the z-direction, which is homogeneous (and thus periodic boundary conditions are required in z). The use of Fourier expansions in one direction yields several significant advantages in our numerical implementations and leads naturally to an efficient mapping on a parallel computer (Chu, Henderson & Karniadakis 1992).

After implementing the Fourier expansions, the dependent variables can be represented as follows:

$$\begin{Bmatrix} u(x,y,z,t) \\ v(x,y,z,t) \\ w(x,y,z,t) \\ p(x,y,z,t) \end{Bmatrix} = \sum_{m=0}^{M-1} \begin{Bmatrix} u_m(x,y,t) \\ v_m(x,y,t) \\ w_m(x,y,t) \\ p_m(x,y,t) \end{Bmatrix} \mathrm{e}^{\mathrm{i}\beta m z}, \tag{2}$$

where the z-direction wavenumber is defined as $\beta = 2\pi/L_z$, and is typically selected on the basis of experimental two-point correlation data. Here L_z is the length of the computational box in the z-direction.

Introducing the Fourier expansions (2) into (1*a*), (1*b*) and taking the Fourier transform (or equivalently, following a Galerkin projection with test functions $\psi_z = \mathrm{e}^{-\mathrm{i}\beta m z}$), we arrive at the discrete-z equivalent of (1*a*), (1*b*),

$$\frac{\partial \boldsymbol{v}_m}{\partial t} + \mathrm{FFT}_m[\mathrm{N}(\boldsymbol{v})] = -\frac{\tilde{\nabla} p_m}{\rho} + Re^{-1}[\nabla^2_{xy} - m^2\beta^2]\,\boldsymbol{v}_m \quad \text{in} \quad \Omega_m, \tag{3a}$$

$$\tilde{\nabla}\cdot \boldsymbol{v}_m = 0 \quad \text{in} \quad \Omega_m. \tag{3b}$$

The computational domain Ω_m is simply an x, y slice of the domain Ω; therefore all the Ω_m are identical. Note that here FFT_m is the mth component of the Fourier transform of the nonlinear terms (denoted by $\mathrm{N}(\boldsymbol{v})$), and that we have introduced the operators $\tilde{\nabla}$, and ∇^2_{xy}, which are defined as

$$\tilde{\nabla} = \left(\frac{\partial}{\partial x}, \frac{\partial}{\partial y}, \mathrm{i}m\beta\right), \qquad \nabla^2_{xy} = \frac{\partial^2}{\partial^2 x} + \frac{\partial^2}{\partial^2 y}. \tag{4a, b}$$

In order to sustain the flow, the momentum equation (1*a*) should include a non-zero pressure gradient in the prevailing direction of motion. In practice, however, the pressure drop is an unknown quantity; this is especially true in complex geometry flows or turbulent flows. It is preferable, therefore, to sustain the fluid motion by imposing a volume (or mass) flow rate $Q(t)$. This can be done efficiently by solving in a preprocessing stage for a Green's function $\boldsymbol{v}^*$ which satisfies the equations of motion for an equivalent Stokes flow that is driven by a unit pressure drop,

$$\frac{\partial v_i^*}{\partial t} = \delta_{i3} - \frac{\partial p^*}{\partial x_i} + Re^{-1}\frac{\partial^2 v_i^*}{\partial x_j^2}, \tag{5}$$

which has an associated flow rate $Q^* = \int_S v_3^*\,\mathrm{d}s$, where S is the cross-sectional area of Ω_m, and the index 3 refers to the flow direction. At subsequent time steps, we then solve the homogeneous Navier–Stokes equations to obtain an intermediate flow field v_i^{H} (with associated flow rate $Q^{\mathrm{H}}(t) = \int_S v_3^{\mathrm{H}}\,\mathrm{d}s$). The requisite non-dimensional forcing term Δp can now be calculated by requiring that the mass flow rate remain at a prescribed level,

$$Q(t) = Q^{\mathrm{H}}(t) + Q^*\Delta p \tag{6}$$

and therefore the final velocity field is given by,

$$\boldsymbol{v} = v_i^{\mathrm{H}} + v_i^*\,\Delta p. \tag{7}$$

2.2. *Numerical methodology*

In this section we will present a brief description of the temporal and spatial discretization procedures of our numerical code. The spectral element–Fourier method has already been employed in similar codes, which have been used in three-dimensional transition studies; see Karniadakis (1990) and references therein for details. Here, for completeness, we will summarize the main ideas in the numerical methodology.

The time discretization of the governing equations (3*a*), (3*b*) employs a high-order splitting algorithm based on mixed explicit–implicit stiffly stable schemes (Karniadakis, Israeli & Orszag 1991; Tomboulides, Israeli & Karniadakis 1989). This splitting algorithm has three major substeps. In the first step, which is explicit, the nonlinear terms obtained for each Fourier component are considered. The next substep incorporates the pressure equation and enforces the incompressibility constraint. Finally, the last substep includes the viscous corrections and the imposition of the boundary conditions. This temporal discretization results in a highly efficient calculation procedure, since it decouples the pressure and velocity equations. The stiffly stable time-splitting scheme is superior to the classical splitting scheme in a number of ways; through its new treatment of the pressure boundary condition, the so-called time-splitting errors that lead to non-zero divergence at Dirichlet boundaries are eliminated (see Tomboulides *et al.* 1989 for details). Accuracy of order J in time (i.e. $O(\Delta t^J)$) is provided (typically we use $J = 3$), in contrast to a classical splitting scheme where only first-order accuracy ($O(\Delta t)$) is achieved, irrespective of the integration schemes involved. The stiffly stable schemes also provide wider stability regions as compared to the more commonly used Adams family schemes (see Karniadakis *et al.* 1991).

The spatial discretization of the governing equations is obtained using the spectral element method (Patera 1984; Karniadakis 1989, 1990). In the standard spectral element discretization, the computational domain is broken up into several quadrilaterals in two dimensions (or general brick elements in three dimensions), which are mapped isoparametrically to canonical squares (or cubes). Field unknowns and data are then expressed as tensorial products in terms of Legendre–Lagrangian interpolants. The final system of equations to be solved is obtained via a Galerkin variational statement. For the current problem under consideration, a hybrid spectral element–Fourier discretization is used for efficiency, owing to the homogeneity of the geometry in the streamwise direction. In this case, two-dimensional spectral elements are used in (x, y)-planes and Fourier expansions are used in the z-direction.

2.3. *Code verification*

A Navier–Stokes solver was implemented using the aforementioned methodology and theory; it is based on direct solvers using a static condensation algorithm to achieve optimal efficiency and speed. Details of the parallel and vectorized serial implementations are given in Chu *et al.* (1992). We will now illustrate the convergence properties of the hybrid spectral element–Fourier method in the following verification test.

The equation

$$\nabla^2 u = f, \tag{8a}$$

with

$$f = \mathrm{e}^{-10\sin(5\pi x)}\,\mathrm{e}^{-y}\,[1 + 2500\pi^2\cos^2(5\pi x) + 250\pi^2\sin(5\pi x)], \tag{8b}$$

has the solution

$$u = \mathrm{e}^{-10\sin(5\pi x)}\,\mathrm{e}^{-y}. \tag{8c}$$

Equation (8*a*) is solved in a two-dimensional x–y slice of the domain pictured in figure 1. This domain is the actual triangular riblet geometry used in the Navier–Stokes computations; details will be presented in §3.1. Dirichlet boundary conditions were used in this test. Figure 2 presents the L_2 and L_∞ errors of the velocity field as a function of the N_{order} employed. We see that spectral accuracy is achieved for this infinitely smooth solution; exponential convergence rates are also obtained in the H_1 norm. We have also undertaken a detailed study to investigate the possibility of numerical problems arising from the *geometrical singularities* presented

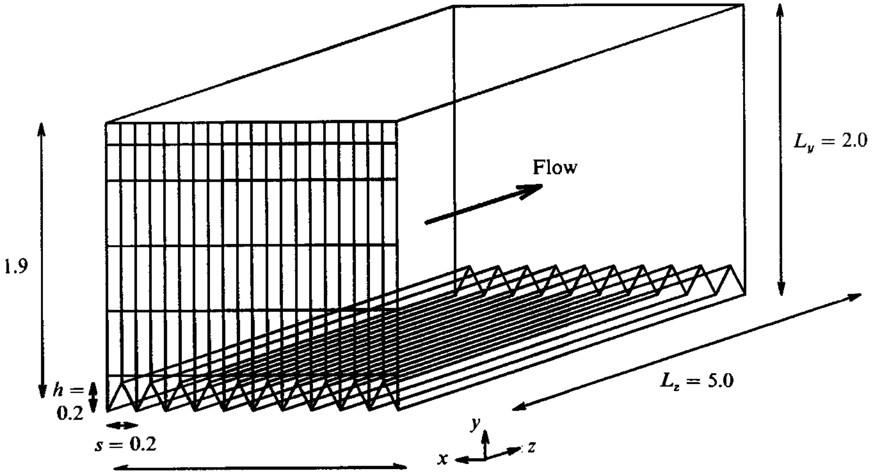

FIGURE 1. Geometry definition and skeleton of the spectral element mesh.

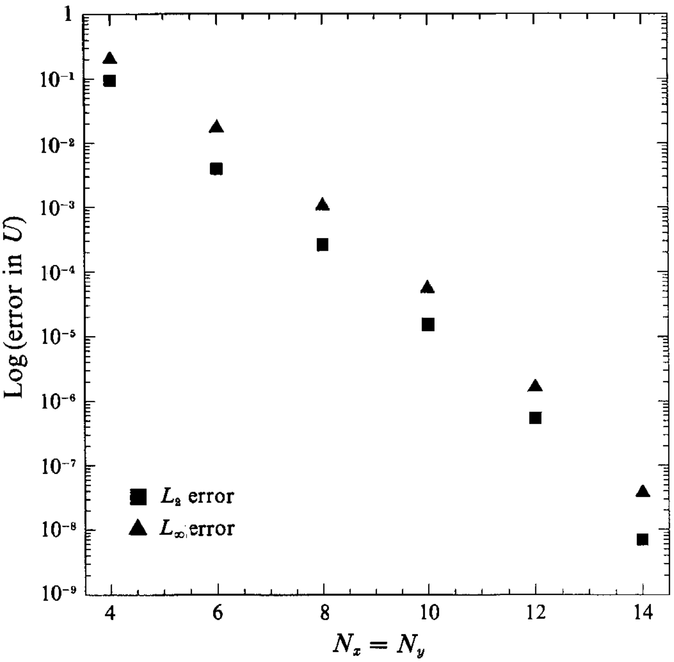

FIGURE 2. Error convergence plot for the Poisson solution.

by the riblet tips. It is well known that the presence of a corner of $\alpha\pi$ radians gives rise to solution with leading behaviour given by $r^{1/\alpha} \sin(\alpha^{-1}\theta)$ where r, θ are the polar coordinates attached to the corner vertex. For the domain of interest here the strongest singularities are caused by the riblet tip where $\alpha = 1.704328$ and thus $u \propto r^{0.58739}$; velocity gradients therefore are unbounded exactly at the tip. This breakdown of analyticity causes a slower convergence around the tip with the error in the H_1 norm decaying as $O(N^{-2/\alpha})$ (Babuska & Suri 1987). This loss of accuracy locally can be treated either empirically by selective h–p mesh refinement as is done here or by auxiliary mappings and singularity subtraction techniques as is explained in detail in Pathria & Karniadakis (work in progress).

The accuracy of the spectral element–Fourier spatial discretization method in the context of the governing equations (1*a*), (1*b*) was tested by solving for an exact solution of the three-dimensional incompressible Navier–Stokes equations. Spectral accuracy was maintained in the L_2 and H_1 norms; details are available in Chu *et al.* (1992).

The computations in this study were performed on a Cray-YMP and on the Intel iPSC/860 Hypercube at Princeton University. We briefly review here the key points of the parallel implementation. In the Intel Hypercube parallel environment, the Fourier decomposition (see (2)) results in some additional benefits. In the context of our temporal discretization, applying a Fourier decomposition in the homogeneous direction yields separate equations for each Fourier mode m with respect to the linear pressure and viscous equations. On a network of parallel processors, the computational domain may then be considered in three steps. In the first step, the domain is mapped in *sheets* of (y, z)-planes, within which FFTs are performed and nonlinear products computed with the processors utilized as a simple array network. During the second phase, the symmetries of the hypercube allow an efficient global transpose (complete exchange) of data across the network so that it arrives as x, y *frames* within processors, where each frame represents a single Fourier mode; during the final phase, the spectral element solvers are applied and the solution is advanced to the next time step. On the Intel iPSC/860 parallel supercomputer, the message passing system operates independently of the microprocessor, allowing an exchange to be initiated while continuing calculations in steps one and three. Thus, on a parallel machine, the final, most expensive step (calling the spectral element solvers) is effectively independent (in terms of required CPU time) of the number of Fourier modes employed. Essentially, for a given amount of CPU time, the number of modes is limited only by the number of processors available.

3. Numerical simulation parameters

3.1. *Computational domains*

The basic geometry in which the incompressible Navier–Stokes equations (1*a*), (1*b*) were solved is depicted in figure 1, along with the coordinate system. The boundary conditions are as follows: periodicity in the x (spanwise) and z (streamwise) directions, and no-slip (walls) in the y (normal) direction. The riblet wall is located at $y = 0$ (triangular riblet tips at $y = 0.2$), and the smooth wall is located at $y = 2.0$. We have chosen a channel with one wall mounted with riblets rather than a flat plate mounted with riblets for a number of reasons. The channel geometry allows us to make simultaneous comparisons of the flow over the top (smooth) wall to the flow over the bottom (riblet) wall, thus eliminating the need to define quantities such as a virtual origin (Bechert & Bartenwerfer 1989), for flat-plate comparisons. Numerically, the periodic domain of the channel is much more accurate and easier to implement than the spatially evolving boundary layer over a flat plate. We also have the added advantages of using momentum balances to check some of the conserved global quantities.

The dimensions of the computational domain were chosen based upon the following factors: (i) dimensions should be large enough to include the expected scales of the largest structures/eddies in the flow, (ii) examination of two-point correlation measurements to ensure that turbulent fluctuations are uncorrelated at separation distances of one half of the periodic length, and (iii) current (and changing) computational restrictions on memory requirements and CPU time. The dimensions of the riblets were chosen such that their dimensions in wall units (at the Reynolds numbers under investigation) would place them in the optimal drag reduction envelopes suggested by experimental studies, as reported by Walsh (1990*a*) and Walsh & Anders (1989). Ideally, one would like to have to consider only factors (i) and (ii) above. However, factor (iii) dictates that we must settle for a 'compromise' between all three factors when choosing a computational domain. For this project, the following computational domain was used: streamwise length $L_z = 5.0$, spanwise length $L_x = 2.0$, and normal length $L_y = 2.0$. This domain has a spanwise wavenumber of $\beta_x = \pi$, which is of the same order as the corresponding value of the most unstable modes in a smooth channel flow (Orszag & Patera 1983). At $Re = 3500$ (a turbulent case), these dimensions in non-dimensional units (based on the smooth-wall values) are roughly: $L_x^+ = 271$, $L_y^+ = 271$, and $L_z^+ = 677$. The triangular riblets are symmetric V-grooves with height $h = 0.2$ and base $s = 0.2$ units in length. At $Re = 3500$, these dimensions correspond to approximately 17.1 viscous wall units (based on riblet wall values); there are 10 riblets across the span of the channel's lower wall.

The Reynolds number in equations (1*a*), (1*b*) is defined as $Re = [W]H/\nu$, where $[W]$ is the bulk streamwise velocity, H is the channel height measured from the midpoint of the riblet to the upper wall, and ν is the kinematic viscosity. The bulk streamwise velocity is defined here as

$$[W] = \frac{1}{S}\iint W(x, y, z_0, t)\,\mathrm{d}x\,\mathrm{d}y, \tag{9}$$

where S is the cross-sectional area of the channel and the integration is performed over this area. H is measured from the riblet midpoint so that (i) it reflects an average value of the distance from the smooth wall to the riblet wall and (ii) it corresponds to the vertical coordinate origin most often chosen in the literature for data normalization purposes (Wallace & Balint 1987; Vukoslavčević *et al.* 1987). For the triangular riblet domain depicted in figure 1, $H = 1.9$.

The early laminar and transitional results of this project were obtained in the computational domain defined above using the following resolutions: $K = 80$, 100 (number of elements), $N_x = N_y = 7$, $N_x = N_y = 9$, $M_z = 8$. These results were validated by simulating the same Reynolds numbers using higher resolutions in N_x, N_y, and M_z (up to $N_x = N_y = 15$, $M_z = 32$); the turbulent regime calculations were then performed. Three different resolutions were tested for the turbulent runs. Each mesh employed the same $N_x = N_y = 9$ and number of Fourier modes $M_z = 16$ before dealiasing; they differed only in the number of spectral elements used (more rows of elements were added near the walls to improve resolution of the turbulent boundary layers). The coarsest mesh (M1) used $K = 100$ elements, the medium mesh (M2) employed $K = 120$ elements, and the finest mesh (M3) used $K = 160$ elements. The x, y spectral element skeletons of these meshes are compared in figure 3. For the M2 mesh, the grid spacings are as follows: in the z-direction 16 symmetric Fourier meshes were employed, corresponding to a streamwise wavenumber of $\beta_z = \frac{2}{5}\pi$, in the x-direction $\Delta x_{\min} = 0.005$, and in the y-direction $\Delta y_{\min} = 0.005$ (near the riblet wall). At $Re = 3500$, these grid spacings correspond to $\Delta x^+_{\min} = 0.43$ and $\Delta y^+_{\min} = 0.42$ in wall units.

For some of the turbulent regime quantities, there were differences between the results obtained with mesh M1 and those computed with mesh M2. There were smaller differences in the statistics results between the M2 mesh and M3 mesh resolutions. In figure 4, we plot the Reynolds stress $-\rho\overline{v'w'}$ profiles across the

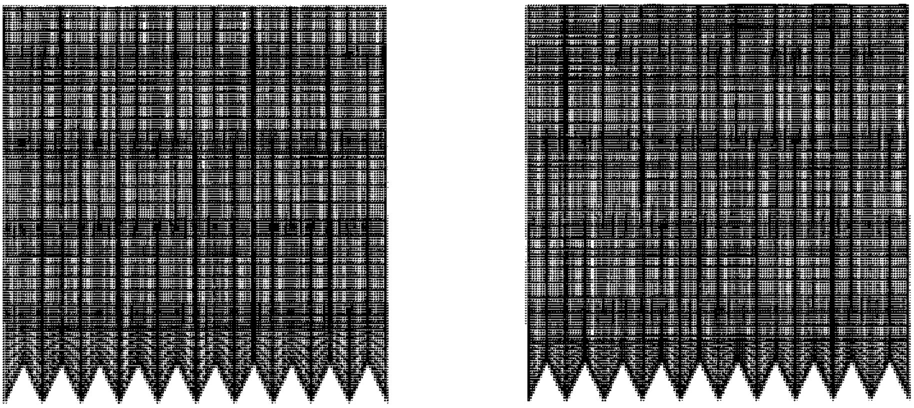

M1 mesh

M2 mesh

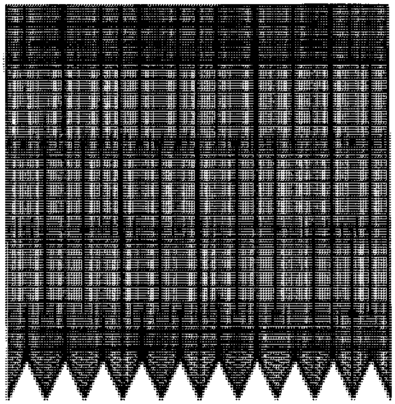

M3 mesh

Figure 3. Comparison of the coarse M1 (100 elements), medium M2 (120 elements), and fine M3 (160 elements) meshes.

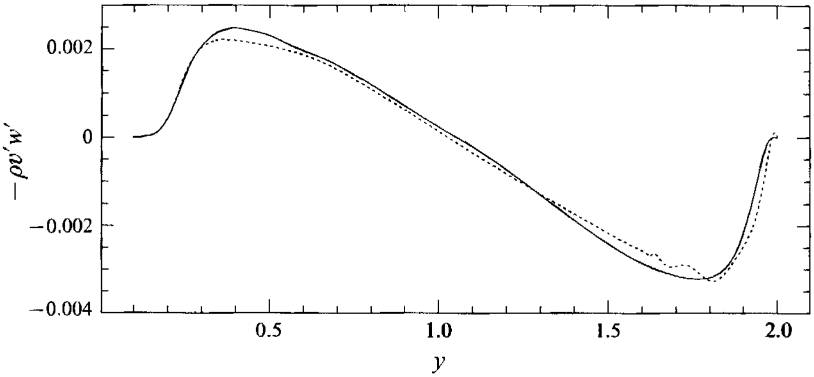

Figure 4. Comparison of $-\rho\overline{v'w'}$ results from coarse ($\cdots\cdot$, $K = 100$) and medium (——, $K = 120$) meshes.

channel (riblet wall on the left, smooth wall on the right) from the M1 and M2 discretizations. For the coarse mesh (M1), we see that although the general profile shape and peak locations are fairly accurate, there are some slight differences. The riblet-wall peak value has been slightly underpredicted, and inadequate resolution near the smooth wall ($1.6 < y < 2.0$) has resulted in numerical oscillations. Because of these oscillations, on the coarse mesh even the sign of $-\rho\overline{v'w'}$ is incorrect in the immediate vicinity of the smooth wall. The M2 discretization has an additional layer of elements placed near the smooth wall – this eliminates the oscillations and yields a smoother profile with the same general shape and peak values. The finest mesh (M3) has two additional layers (added to the medium mesh) of elements, one placed at the riblet wall, the other placed at the smooth wall; no significant changes resulted.

Owing to the larger computational costs of the M3 mesh (33.7 Mwords on the Cray-YMP as compared to 25.3 Mwords for the M2 mesh, when run in core memory), the majority of the simulations and turbulence statistics calculations were obtained on the mesh corresponding to $K = 120$, $N_x = N_y = 9$, and $M_z = 16$. Unless otherwise noted, flow simulation results presented in the following sections correspond to this resolution. Higher (N_x, N_y) were used for some of the laminar regime test to examine non-uniform convergence near the riblet tips. Recent results using the same spectral element mesh with $M_z = 32$ modes have shown small differences; past channel flow computations (Kim, Moin & Moser 1987; Zores 1989) have demonstrated that the streamwise direction is the most 'forgiving' in terms of resolution. Recent findings by Zores (1989) demonstrate that spectral methods can sustain turbulence and predict statistics with reasonable accuracy in channel flow with as few as four Fourier modes in the streamwise direction. Given the limited computational resources available, we have thus decided to concentrate numerical resolution in the spanwise and normal directions of our domain.

Section 4.6 will present some preliminary results obtained from a simulation of flow over slightly rounded riblets. The computational domain described earlier was modified slightly; all dimensions and resolutions remained unchanged except for the actual riblet dimensions. The symmetric rounded riblets have height $h = 0.18$ and base $s = 0.2$ units in length; these correspond to $h^+ \approx 18.3$ and $s^+ \approx 20.3$ at $Re = 3500$. The curvature of the riblet tip (the lower half of the riblet is virtually unchanged) corresponds to a smooth spline fit that attempted to match the slope of the original riblet near the midpoint. The new channel height for the rounded-riblet domain is $H = 1.91$.

3.2. *Transition to turbulence*

All the riblet simulations were performed with a constant volume flow rate of $Q(t)$ equal to the cross-sectional area of the computational domain, thus fixing the bulk streamwise velocity at $[W] = 1.0$ (see the end of §2.1 for details). For the triangular riblets a constant flow rate of $Q(t) = 3.8$ was used, whereas for the rounded riblets, $Q(t) = 3.802657778$.

A number of different perturbations were investigated in an attempt to trip the initial flow (the laminar steady-state solution). Disturbances of low to moderate amplitude imposed on (x, y)-planes and uniform along the streamwise direction (z) died out. The disturbance form that produced the best results corresponded to superimposing a large-amplitude streamwise sinusoidal wave onto the mean velocity field. This perturbation contained energy in only some of the higher Fourier modes (modes 2–5) and had an amplitude equal to 10% of the mean bulk velocity; disturbance waves with amplitudes less than 10% all failed. Amplification of the

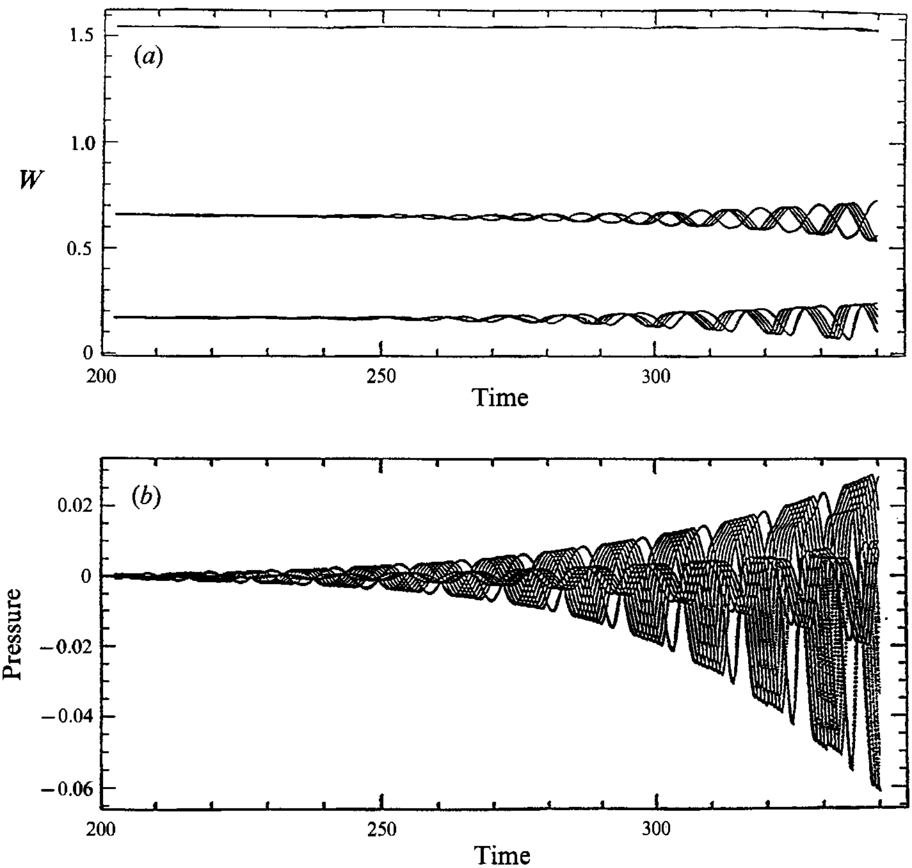

FIGURE 5. Exponential amplification of the initial disturbance ($Re = 3500$); (a) W and (b) P soon after the perturbation.

disturbance occurred and the simulation was carried out for a large number of convective time units ($H/[W]$). We note that Zores (1989) reported that a disturbance of amplitude 30% of the mean was necessary in order to promote transition in a lower-resolution channel flow spectral simulation.

Figure 5 shows time histories (from various fixed points in the domain in physical space) of the streamwise velocity and pressure soon after the initial perturbation at $Re = 3500$; we see the onset of exponential amplification of the disturbance. Increasing amounts of energy are introduced into the higher (non-zero) Fourier modes at later times.

The equations were integrated forward in time for a large amount of convective time units, until eventually a stationary turbulent flow was reached. We identified the time-independence of this statistically steady flow state (and began tracking turbulence statistics) when the following conditions were satisfied: (i) the total shear stress profile became linear (see §4.3 for details), (ii) the mean velocity profile over the smooth wall agreed with the 'law of the wall' (see §4.2 for details), and (iii) examination of the time histories and spectra of instantaneous quantities verified the disappearance of intermittency.

In the subcritical cases (in the laminar regime) the initial disturbance died out, as shown in figure 6(a), which is a time history of the streamwise velocity at a single

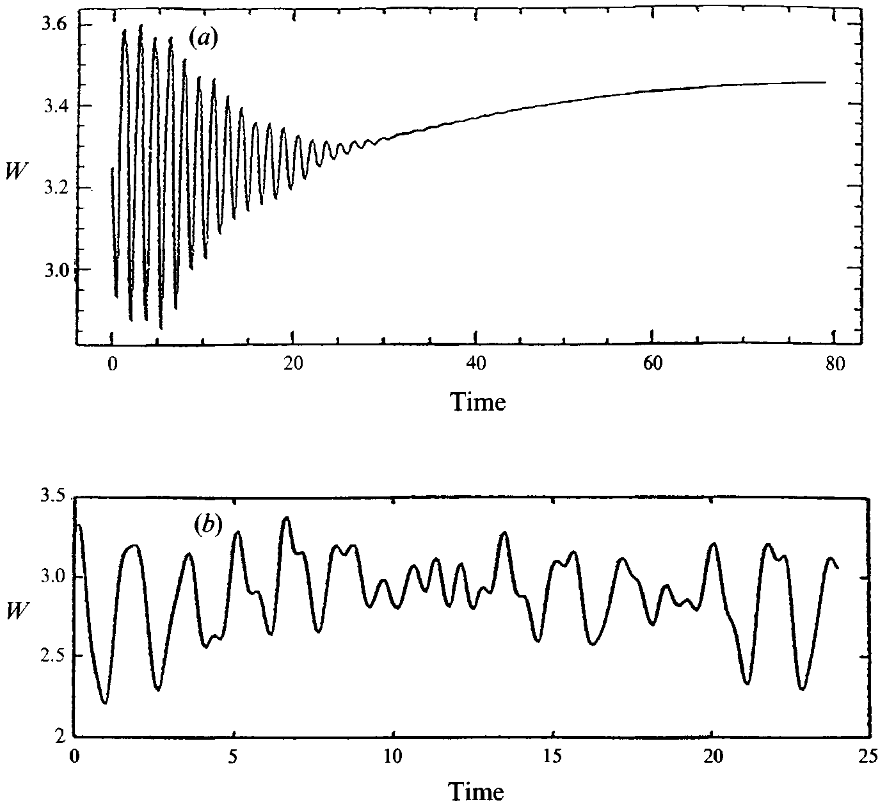

FIGURE 6. Time histories of the streamwise velocity at single fixed points in the domain: (*a*) subcritical case – disturbance dies out and the flow returns to its laminar steady state ($Re = 1500$), (*b*) flow is transitional ($Re = 2750$).

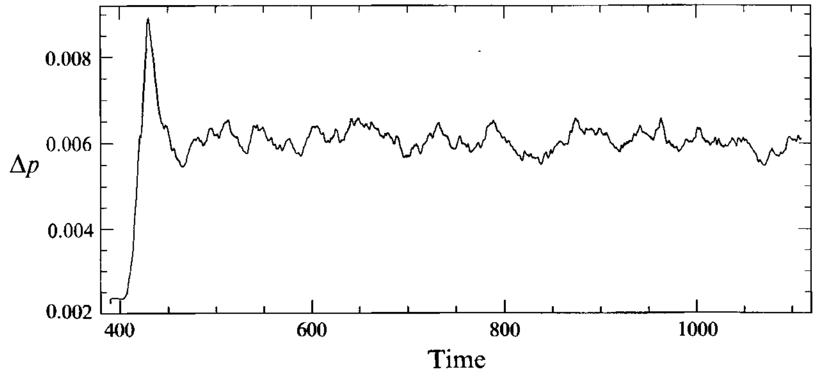

FIGURE 7. Instantaneous pressure drop history reaches a statistically steady state ($Re = 3500$).

point in the flow. In figure 6(*b*), a transitional state is reached. The perturbation does not die out, but inadequate resolution (this result is from the $K = 80$, $N_x = N_y = 7$ case) prevents further evolution to a turbulent state.

The higher-resolution meshes allowed us to compute the essential (smaller) turbulence scales and the flow was further integrated until a stationary state was finally achieved. Figure 7 is a time history of the non-dimensional pressure gradient (Δp from (7)), shown some time after passing through transition (the large over-shoot spike in the signal). A stationary state has been reached by approximately $t = 600$ (in the non-dimensional time units of figure 7). We note that this non-dimensional forcing term oscillates with an amplitude of roughly 8%, and that it contains numerous high- and low-frequency fluctuations.

4. Results

4.1. *Laminar flow results*

Steady, time-independent solutions corresponding to fully developed laminar flow were obtained in the computational domain depicted in figure 1. In figure 8, we consider profiles of the streamwise velocity at $Re = 1000$, in global coordinates. Three profiles are shown, taken across the channel from the riblet valley, midpoint, and tip locations to the smooth wall. The laminar velocity profiles in the riblet channel are similar to the parabolic profile of a plane Poiseuille flow, except in the riblet valley regions. We see that above $y \approx 0.3$, all profiles collapse to the same result. Inside the riblet valleys, however, the streamwise velocity profiles are inflexional in nature – in the laminar regime this is the main difference between the flow over the smooth wall and the flow over the riblet wall. The presence of an inflexion point in the velocity profile suggests that the instability mechanism which initiates transition over the riblets may be different from that of the smooth wall. This is one of the many crucial issues that need further investigation if riblets are to be considered in industry applications (Lynch & Klinge 1991; Robert 1992). Fundamental understanding of how riblets affect flow stability and transition properties in complex geometries is needed. Ongoing and future research in this project will address such transition studies; currently, such a detailed investigation using direct numerical simulation (DNS) alone is prohibitively expensive.

The inflexional velocity profiles inside the riblet valleys identify regions of slow-moving fluid near the wall (compared to the regions near the riblet tips), and thus correspond to regions of lower shear stress. In figure 9, we examine the distribution of the local skin friction inside a typical riblet valley in the laminar regime (at $Re = 1000$). We define the local skin friction and wall shear stress as

$$C_f = \frac{\tau_w}{\frac{1}{2}\rho[W]^2}, \qquad \tau_w = \mu\frac{\mathrm{d}W}{\mathrm{d}n}, \tag{10a, b}$$

where n is the direction normal to the wall surface (for the smooth wall, $n = y$).

In this figure, the triangles correspond to C_f at collocation points along the valley wall. Note that the regions near the riblet tips have a higher shear stress than the smooth wall, while the valley locations have a decreased shear stress. While the riblet wall has a lower average skin friction ($C_{f_{\mathrm{riblet}}} = 0.00592$) than that of the smooth wall ($C_{f_{\mathrm{smooth}}} = 0.01284$), its *drag* (which depends on the wetted area) is higher. For the symmetric triangular riblets, the ratio of lower-wall surface area to top-wall surface area is $A_{\mathrm{riblet}}/A_{\mathrm{smooth}} = 2.23607$; this yields a drag penalty for the riblet wall at this Reynolds number.

In the laminar flow regime, the C_f profiles in the riblet valleys are self-similar at each Reynolds number; the riblet wall always has a higher drag than the smooth wall for laminar flow (see figure 33 in §4.5). For steady, fully developed, laminar flow in a channel with two smooth walls, the exact relation of the wall skin friction to the Reynolds number can be derived as: $C_f = 12/Re$. The steady-state laminar solution corresponding to the flow in our particular riblet channel (using the triangular

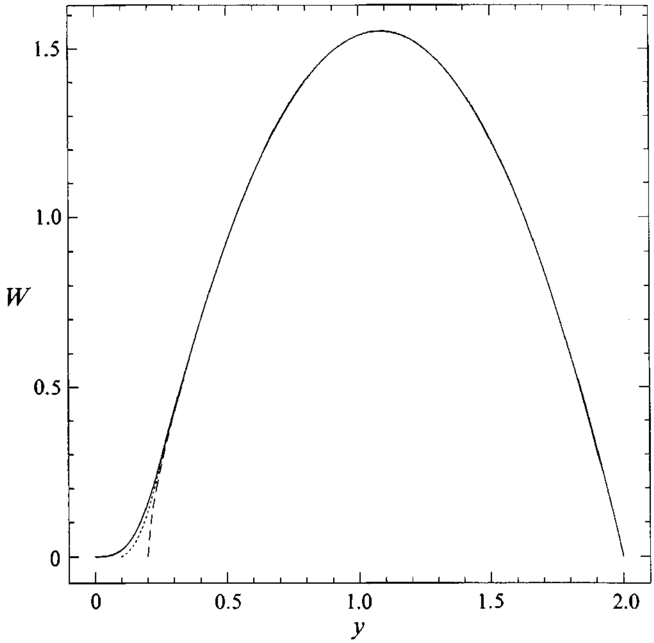

FIGURE 8. Laminar streamwise velocity profiles across the triangular riblet channel in global coordinates, at $Re = 1000$: ——, valley; · · · · ·, midpoint; – – –, tip.

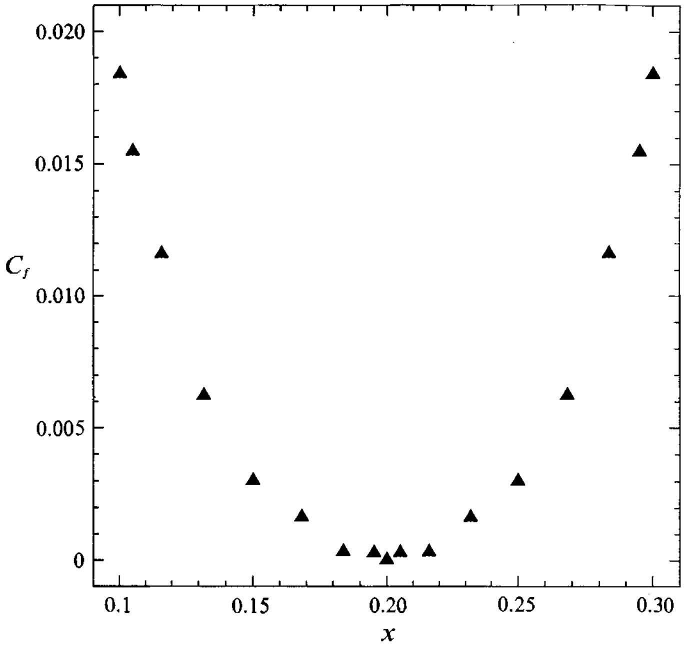

FIGURE 9. Distribution of local skin friction inside a triangular riblet valley at $Re = 1000$.

riblets) is similarly fully developed; the only non-zero velocity component in the solution is the streamwise velocity W. Therefore, we may empirically derive an expression for the *average* skin friction on the riblet wall, $C_f \approx 5.92/Re$, which is valid for the lower wall of our channel in the laminar regime. Thus, there will not be any

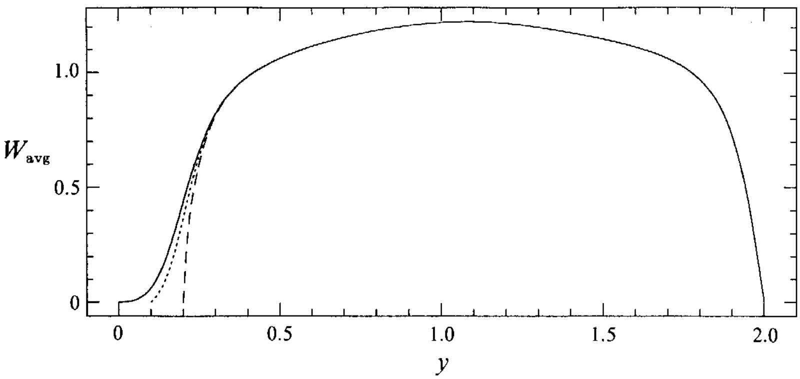

FIGURE 10. Mean streamwise velocity profiles in global coordinates through the riblet valley (——), from the riblet midpoint (· · · · · ·), and from the riblet peak (– – – –).

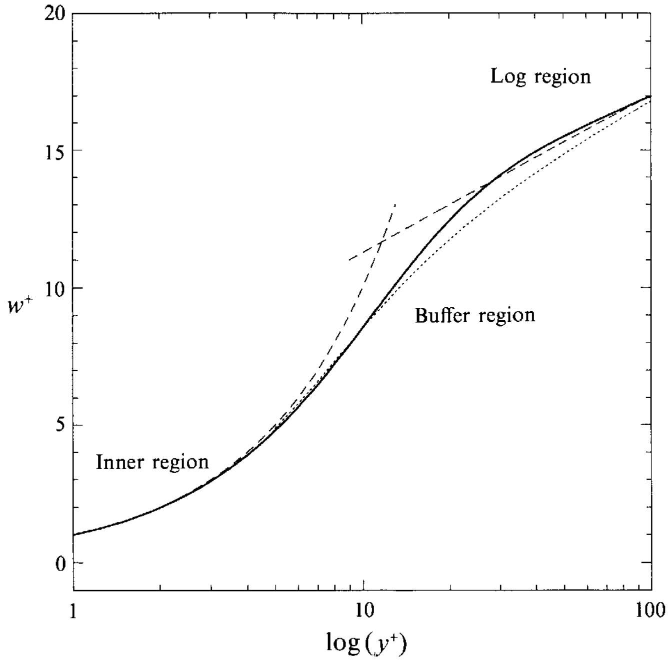

FIGURE 11. Mean streamwise velocity profile above the smooth wall in wall coordinates: ——, computed values; – – – –, linear and log laws; · · · · ·, Spalding's law of the wall.

drag reduction in laminar flow for the triangular riblets we consider. The character and general profile of the local skin friction distribution (highest at the tips, lowest in the valley) is similar for flows in the turbulent regime (see §4.5 for details).

4.2. *Turbulent mean flow properties*

In figure 10 three profiles of the mean streamwise velocity at $Re = 3500$ are shown in global coordinates. They are taken from three different points on the riblet wall (from the riblet valley, from the midpoint, and from the riblet tip) to the smooth wall. As with the laminar flow results of §4.1, the profiles inside the riblet valley are inflexional. Below the midpoint of the riblet valley, the mean streamwise velocity does not exceed 5% of the bulk velocity. We see that the influence of the riblet wall on the velocity profile extends upwards to approximately $y \approx 0.3$ ($y^+ \approx 26$ in riblet wall units) for this Reynolds number; above this point the profiles from the three different regions collapse to a single profile.

In figure 11, we examine the mean streamwise velocity profile above the top (smooth) wall in non-dimensional wall coordinates. The dashed and dotted lines correspond to:

$$w^+ = y^+, \tag{11a}$$

$$w^+ = (1/\kappa)\ln(y^+) + \beta, \tag{11b}$$

$$y^+ = w^+ + \mathrm{e}^{-\kappa\beta}[\mathrm{e}^{\kappa w^+} - 1 - \kappa w^+ - \tfrac{1}{2}(\kappa w^+)^2 - \tfrac{1}{6}(\kappa w^+)^3]. \tag{11c}$$

Equation (11*a*) represents the linear region, and (11*b*) represents the logarithmic region (both are represented with dashed lines). The dotted line is (11*c*): Spalding's law of the wall. All three equations are depicted using Nikuradse's values of $(\kappa, \beta) = (0.40, 5.5)$, which are more appropriate for this low Reynolds number flow. The computed mean streamwise velocity profile above the smooth wall is represented by the solid line. It is in excellent agreement with the suggested correlations. The corresponding mean velocity profile above the riblet wall is shown in figure 12; the dashed and dotted lines are again (11*a–c*), and the solid line represents the computed values. Here, the valley midpoint has been chosen for the origin $y^+ = 0$ and a span-averaged value of the *local* shear velocity is used for normalization. The riblets seem to effectively thicken the viscous sublayer; the upward shift in the logarithmic region reported by Wallace & Balint (1987) is clearly evident here, although it is overpredicted. This quantitative difference is perhaps due to a different normalization with respect to the shear velocity.

Additional bulk flow properties have been computed; those corresponding to $Re = 3500$ (for the triangular riblet domain) are listed in table 1. It is interesting to compare the smooth-wall and riblet-wall values to each other, and to empirical correlations from Dean (1978), who presents an extensive survey of experimental high aspect ratio (two-dimensional) channel bulk flow parameters. It should be noted, however, that Dean's correlations are for smooth channels (with two flat walls) at higher Reynolds number regimes than those investigated in this study; caution should be exercised when making comparisons. Recent numerical and experimental studies in smooth-channel flows suggest that fluid from one wall does not contribute significantly to the Reynolds shear stress at the opposite wall for geometries of similar dimensions to the one under consideration (see Antonia *et al.* 1992). However, there was no attempt in the current study to investigate this issue, which should be addressed in future work.

For the riblet channel at $Re = 3500$, the values of the Reynolds number based on centreline velocity and shear velocity are $Re_c = 2250$, $Re_\tau = 131$ for the smooth wall, and $Re_\tau = 128$ (based on the span-averaged shear velocity) for the riblet wall. Here $Re_c = W_c(\frac{1}{2}H)/\nu$ and $Re_\tau = W_\tau(\frac{1}{2}H)/\nu$. Dean suggests a ratio of centreline velocity to bulk velocity of $W_c/[W] = 1.28 Re^{-0.0116}$ for a smooth channel in the regime $6 \times 10^3 < Re < 6 \times 10^5$. This equation yields a ratio of 1.16 at $Re = 3500$; the computed ratio for the riblet channel is 1.22. This value of $W_c/[W]$, however, compares more favourably with the experimental results reported in Dean (1978) if we consider the proper regime $3000 < Re < 6000$. At $Re = 3500$, the experimental data from Dean (1978) correlates with $W_c/[W] = 1.21$, indicating much better agreement. It should

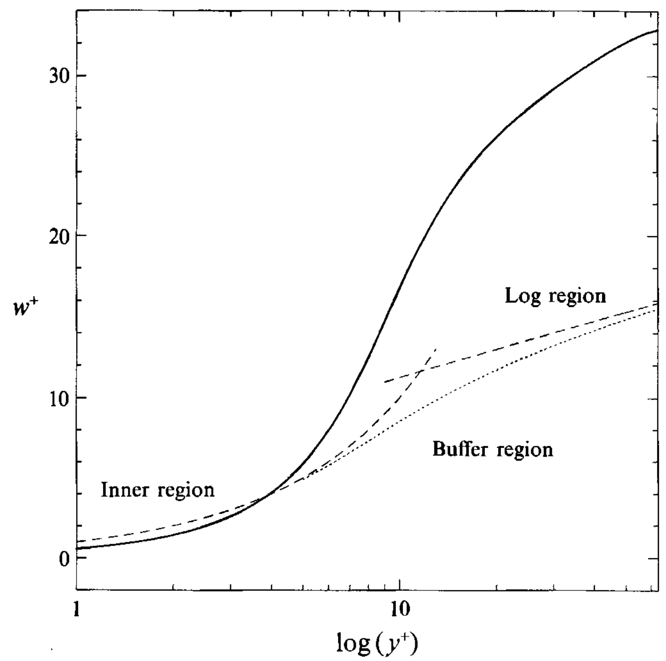

FIGURE 12. Mean streamwise velocity perturbation above the riblet wall (midpoint location) in wall coordinates. Notice that non-dimensionalization is performed with the *local* shear velocity. Curves defined as in figure 11.

	Smooth wall		Riblet wall
Re		3500	
Re_c		2250	
Re_τ	131		128*
$W_c/[W]$		1.22	
W_c/W_τ	17.08		17.54*
δ^*	0.140		0.205
θ	0.079		0.089
$H = \delta^*/\theta$	1.77		2.30
$G = \dfrac{W_c}{W_\tau}\left(\dfrac{H-1}{H}\right)$	7.45		14.85
$J = \dfrac{W_c - [W]}{W_\tau}$	3.08		4.74

TABLE 1. Comparison of bulk flow properties for the triangular riblet domain. * Based on span averages.

also be noted that the presence of the riblet wall should be expected to yield a slightly different centreline velocity for the riblet channel as compared to a smooth channel.

The following quantities all depend on the displacement thickness δ^* and the momentum thickness θ; there is some uncertainty, however, concerning how relevant these values are for the riblet wall, since its geometry varies in the spanwise and normal directions, and the location of the normal origin is somewhat arbitrary. To be consistent with the choice of H (see §3.1) and the literature, measurements for the riblet wall are based on a normal coordinate origin located at the riblet valley midpoint ($y = 0.1$). We may then use the following results to provide us with insight into the 'overall effect' of the riblet wall, and we use Dean's correlations to help us in estimating the accuracy of the smooth-wall calculations.

The displacement thicknesses for the smooth wall and riblet wall are $\delta^*_{\text{smooth}} = 0.140$ and $\delta^*_{\text{riblet}} = 0.205$. As expected, the riblet wall has a much larger (by approximately 46%) δ^*, which would correspond to a lower shear stress on an identical geometry. The values of momentum thickness are $\theta_{\text{smooth}} = 0.079$ and $\theta_{\text{riblet}} = 0.089$. Again, the riblet wall has a larger (by approximately 13%) value of θ than the smooth wall, consistent with the lower shear stress trend.

Typical values of the shape factor $H = \delta^*/\theta$ range from 1.2 (for a boundary layer in an accelerating flow) to 3.5 (for a boundary layer on the point of separation) (Dean 1978). The value of H for the smooth wall is $H_{\text{smooth}} = 1.77$; this compares well to Dean's empirical result of $H = 1.76$ for $Re = 3500$. The shape factor for the riblet-wall boundary layer is $H_{\text{riblet}} = 2.3$; this larger value is consistent with the profiles depicted in figure 10. The Clauser shape parameter G, which is a shape factor that remains constant in an equilibrium turbulent boundary layer (H may vary with z), is given by

$$G = \frac{W_c}{W_\tau}\frac{H-1}{H}. \tag{12}$$

Dean's data yield a value of $G = 7.1$ (for $Re = 3500$); the riblet channel has the values $G_{\text{smooth}} = 7.45$ and $G_{\text{riblet}} = 14.85$. The velocity defect ratio $J = (W_c - [W])/W_\tau$ is typically used to describe profile similarity outside the viscous sublayer. For $Re = 3500$, Dean's empirical correlation is $J = 3.1$; our computations show $J_{\text{smooth}} = 3.08$ and $J_{\text{riblet}} = 4.74$.

The non-dimensionalized triangular riblet dimensions h^+, s^+ (height, base) for $Re = 3500$ are 17.1 wall units based on the shear velocity averaged over the valley or 25.5 based on an equivalent shear velocity averaged over the riblet span. We see that the riblets are in the optimal drag-reduction envelope of approximately $5 < (h^+, s^+) < 30$ for symmetric V-groove riblets, as investigated in Walsh (1990*b*) and Walsh & Anders (1989).

4.3. *Turbulence statistics*

In this section, we discuss the statistical data that have been gathered from the turbulent flow results at Reynolds number 3500. Our results include low-order and higher-order statistics involving all three velocity components, and are examined using both spatial and temporal analyses. The statistics were computed over a time sample of roughly 300 non-dimensional time units; in the following sections an overbar will correspond to a time-averaged quantity. Where appropriate, all statistical quantities have been additionally averaged in z (the homogeneous direction), and also horizontally 'piecewise-averaged' in x (the spanwise direction), thus collapsing the domain to one single riblet for analysis of the averaged statistics (the overbar notation is also used for these averages).

4.3.1. *Correlations and turbulence intensities*

The spanwise two-point correlation functions for each component of the fluctuation velocities have been computed and are examined below. The streamwise velocity correlations are defined by

$$R(y,r)_{ww} = \frac{\overline{w'(x,y,z)\,w'(x+r,y,z)}}{\overline{w'(x,y,z)}^{2}}, \tag{13a}$$

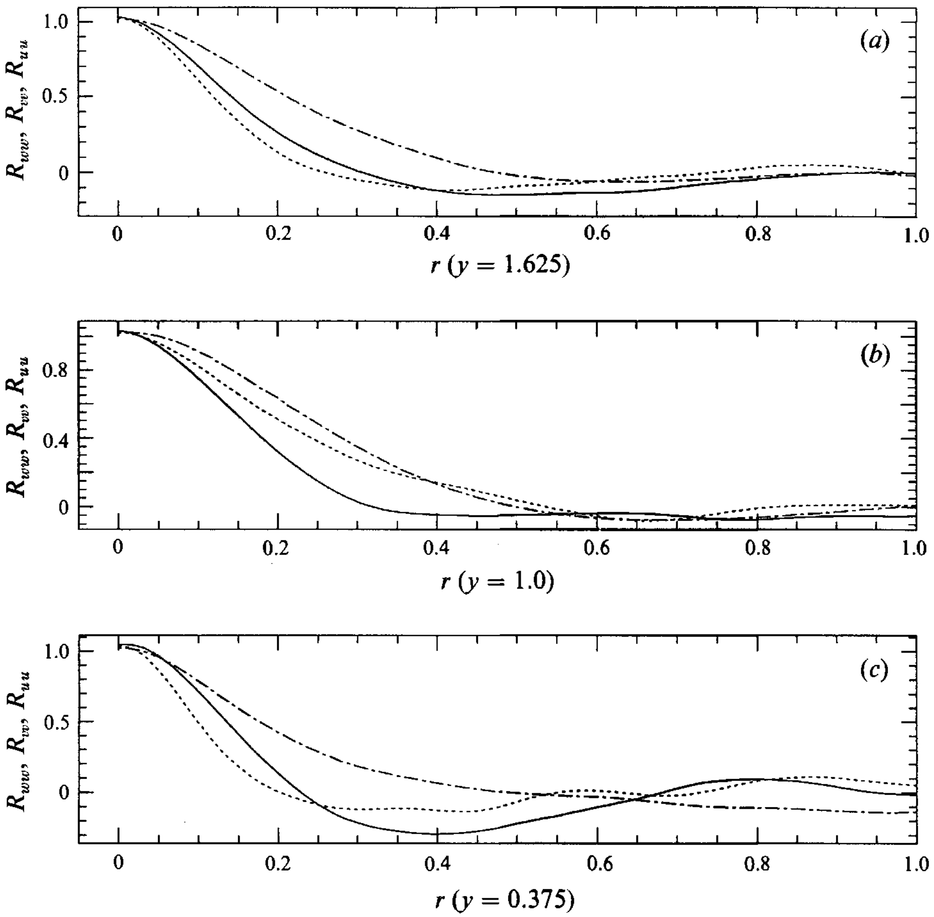

FIGURE 13. Spanwise two-point velocity correlations (*a*) near the smooth wall, (*b*) close to the centreline, and (*c*) near the riblet wall. ——, R_{ww}; · · · ·, R_{vv}; —·—·—, R_{uu}.

and $R(y,r)_{vv}$, $R(y,r)_{uu}$ are defined similarly. As was mentioned in §3.1, the computational domain should be large enough so that turbulent fluctuations are uncorrelated at separation distances of one half of the periodic length(s) of the domain. Figure 13 shows examples of two-point correlations in the spanwise direction at three y-locations: (*a*) at a point near the smooth wall ($y = 1.625$), (*b*) close to the channel centreline ($y = 1.0$), and (*c*) at a point near the riblet wall ($y = 0.375$). The three velocity correlations have been overlaid in each plot. In all cases, the correlations approach zero for increasing separation distances, indicating that the spanwise length of the computational domain ($L_x = 2.0$) is sufficiently large. There appears to be an anomaly in the R_{uu} plot, which seems to approach a non-zero value. This may be due to an inadequate time sample; unfortunately, for this geometry no experimental data on spanwise correlation length are available. It is interesting to note that there is actually a pronounced negative w'-correlation near the riblet wall (see figure 13*c*). Current computational resources have limited the streamwise extent of the computational domain to $L_z = 5.0$, or about 680 viscous wall units at $Re = 3500$. Profiles of quantities in the streamwise direction are modulatory and consist of up to five complete waves.

The computed turbulence intensities, ($w_{\mathrm{rms}} = (\overline{w'^2})^{\frac{1}{2}}$) etc., are shown in figures 14,

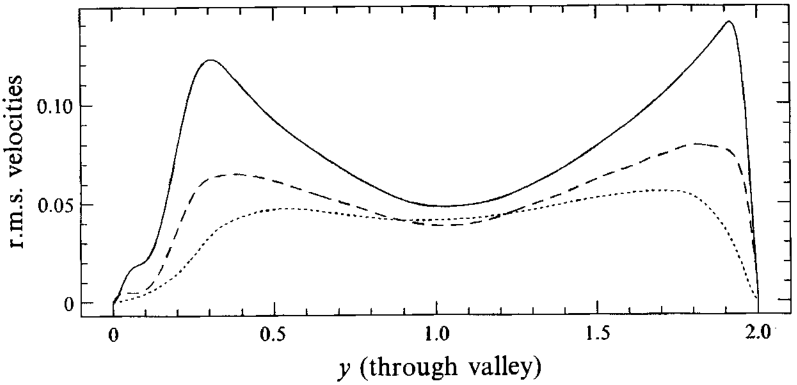

FIGURE 14. The three components of the turbulence intensities through the riblet valley. The riblet wall is located on the left (at $y = 0$ to 0.2) and the smooth wall is located on the right (at $y = 2.0$). ——, w_{rms} (streamwise); · · · ·, v_{rms}; – – –, u_{rms} (spanwise).

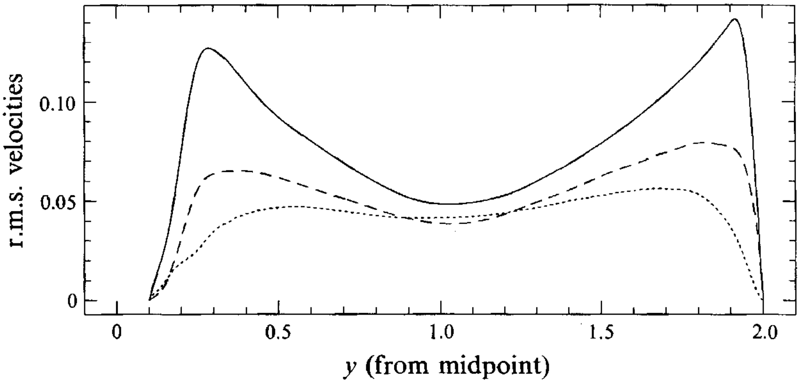

FIGURE 15. As figure 14 but from the riblet midpoint.

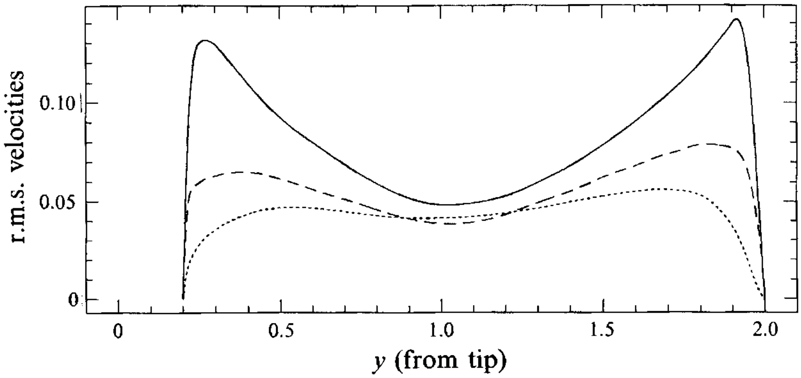

FIGURE 16. As figure 14 but from the riblet tip.

15, and 16, where the three components of the velocity fluctuations are normalized by the bulk streamwise velocity. Profiles are taken across the channel (with the riblet wall on the left and the smooth wall on the right) at spanwise locations through the riblet valley ($y = 0$), from the riblet midpoint ($y = 0.1$), and from the riblet tip ($y = 0.2$).

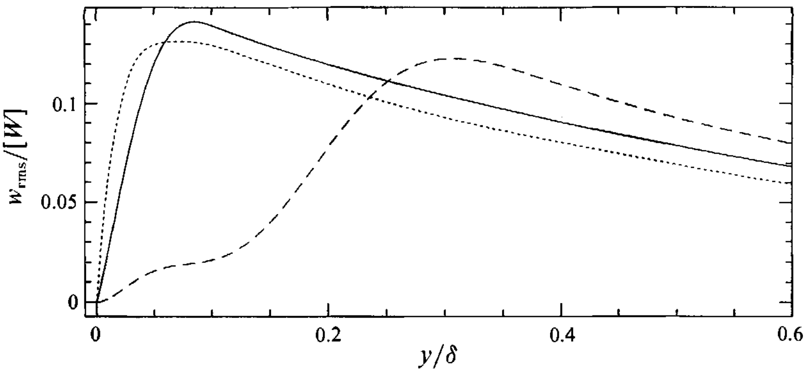

FIGURE 17. Streamwise turbulence intensity in the near-wall region: ——, smooth wall; · · · · ·, riblet tip; – – –, riblet valley.

The profile shapes and peak values of the turbulence intensities above the smooth wall are in good agreement with turbulent channel flow results, both experimental and computational results of Kim *et al.* (1987), Gupta & Kaplan (1972), and Kreplin & Eckelmann (1979). The streamwise intensity values above the riblet wall are in good agreement with the experimental results reported in Walsh (1990*a*), Wallace & Balint (1987), Vukoslavčević *et al.* (1987), and Choi (1989), which correspond to flows over riblet-mounted flat plates; no experimental results for riblet-mounted channel flows exist, and no other computational results (apart from those in this present study) for turbulent flow over riblets have been obtained yet. Only a few investigators have measured the normal and spanwise fluctuations over riblets (over a riblet-mounted flat plate), i.e. Choi (1989), Walsh (1980), and Hooshmand (1985); these results have been inconclusive, showing either no change or small reductions over the boundary layer. The inconsistencies between the experimental data and the smaller values of the normal and spanwise fluctuations make it likely that these measurements have been affected by probe error (cross-contamination of hot-wire probes greatly affect normal and spanwise measurements, for instance), see Walsh (1990*a*). Recently, new experimental data (LDV measurements) for spanwise fluctuations over riblets have been obtained by Benhalilou *et al.* (1991); these are in good agreement with our simulation results.

From figures 14, 15, and 16, it is apparent that all three components of the turbulence intensities are reduced in the vicinity of the riblet wall (compared to values near the smooth wall), even at locations above the riblet tips, in agreement with the findings of Vukoslavčević *et al.* (1987). This is an interesting phenomenon, in the light of the fact that the local wall shear is substantially higher than near the riblet tips when compared to the smooth-wall values; these details will be discussed in §4.5. We also note that the profiles of the streamwise and spanwise r.m.s. velocities taken from the riblet valley show slight bumps deep in the valley regions; this will also be discussed at further length in later sections.

To investigate the differences between the smooth- and riblet-wall profiles in more detail, we examine profiles of the streamwise turbulence intensity near the wall in figure 17. Profiles from the smooth wall, the riblet tip, the riblet midpoint, and the riblet valley have been overlaid and shifted such that the plot origin ($y/\delta = 0$) corresponds to the wall surface of each profile. Here δ is the channel half-height defined earlier. We see that the presence of the riblets reduces the peak streamwise velocity fluctuations as compared to the smooth wall; at the valley location there is

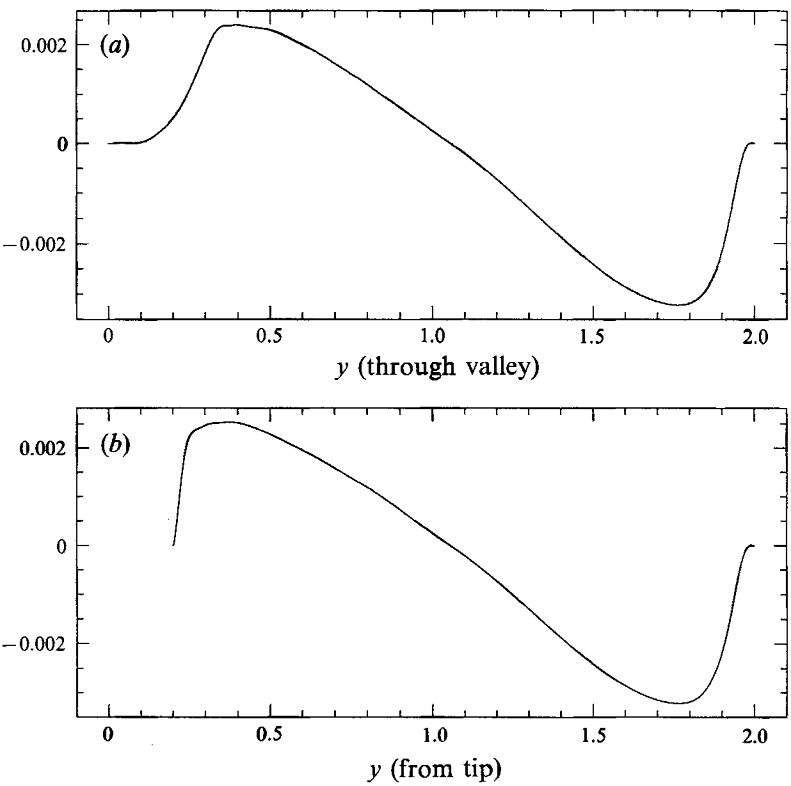

FIGURE 18. $-\rho\overline{v'w'}$ (streamwise) component of the Reynolds stress across the channel (riblet wall on the left, smooth wall on the right); (a) through valley, (b) from tip.

an approximate reduction of 11 %. The turbulence intensity is effectively suppressed inside the valleys of the riblets ($y/\delta < 0.2$). Near the bounding surface of the smooth wall, the streamwise intensity peaks at roughly 14 % of the bulk streamwise velocity, while the intensity above the riblet valley locations reaches only 7 % at $y/\delta = 0.2$. It is interesting to note, however, that although very low, the turbulence intensity levels inside the riblet valleys are not negligible. The small bump in the w_{rms} profile at $y/\delta \approx 0.05$ (and the small bump in the u_{rms} profile) suggests slight activity even in regions deep within the riblet valleys; this further confirms the need for full Navier–Stokes simulations of riblet flows, and is consistent with the flow reversal findings reported in §4.4.2.

4.3.2. *Reynolds shear stress*

Experimental results to date have shown contradicting measurements of the Reynolds stress in flow over riblets; most investigators (Walsh 1990*b*) have found a reduction over the entire boundary layer, while some (Hooshmand 1985) have reported an increase for locations near the riblets. These discrepancies are most likely due to the same uncertainties involved in hot-wire measurements of the normal and spanwise turbulence intensities.

In figure 18 we plot the $-\rho\overline{v'w'}$ component of the Reynolds stress across the channel. As in figure 14, the riblet wall is on the left and the smooth wall is on the right of the plot; profiles are taken from spanwise locations (*a*) through the riblet valley and (*b*) at the riblet tip. The profile shapes and peak values above the smooth

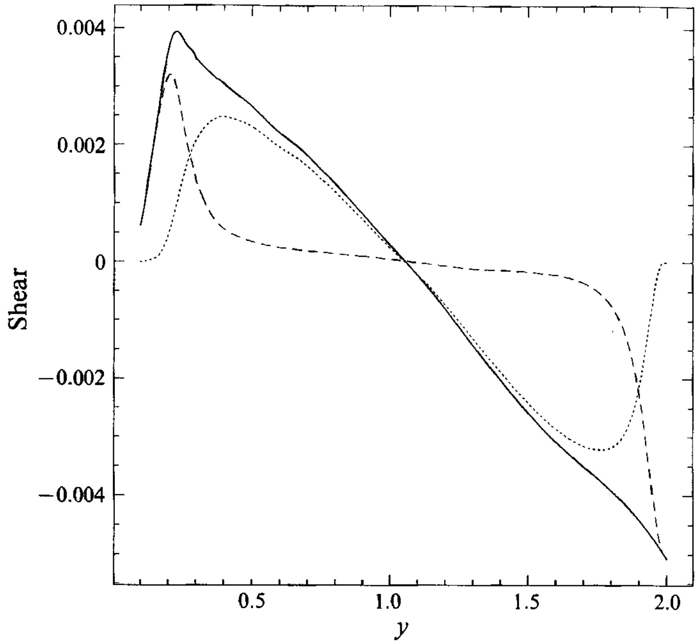

FIGURE 19. Total shear across the channel, in global coordinates. Profiles are taken from the riblet midpoint. ——, Total shear; – – –, $\mu \mathrm{d}W/\mathrm{d}y$; · · · · ·, $\rho \overline{v'w'}$.

wall are in good agreement with turbulent channel flow and flat-plate results (Wallace & Balint 1987; Gupta & Kaplan 1972). Detailed experimental and/or computational Reynolds stress profiles over riblets at specific stations are not available (aside from those presented here).

It is apparent that the riblets significantly reduce the Reynolds stress values, as compared to the smooth wall, and thus result in decreased vertical momentum transport. This is consistent with our findings of drag reduction at this Reynolds number (see §§4.4 and 4.5 for details). The peak $-\rho\overline{v'w'}$ value is reduced by more than 20% above the riblet wall. We also note that figure 18 shows that virtually zero vertical momentum transport occurs inside the valleys of the riblets.

In fully developed turbulent channel flow, we expect that the total shear stress $\tau_{\mathrm{total}} = \mu(\mathrm{d}\overline{W}/\mathrm{d}y) - \rho\overline{v'w'}$ will be linear across the channel (for a channel with two smooth walls) when the flow reaches an equilibrium state. As mentioned in §3.2, this profile was used to establish the point in the time integration when the flow had reached a statistically steady state. In figure 19, τ_{total} is plotted across the channel from a spanwise location corresponding to the riblet midpoint – hence the deviation from a straight line near the riblet wall. The solid line is the total shear, while the dashed line represents the physical shear $\mu(\mathrm{d}\overline{W}/\mathrm{d}y)$ and the dotted line is the Reynolds stress component $-\rho\overline{v'w'}$. We see that across most of the channel the total shear is linear, and that it falls dramatically inside the riblet valley; this is consistent with our other findings of substantially reduced Reynolds stresses and wall shear inside the riblet valleys.

4.3.3. *Quadrant analysis*

A quadrant analysis of the Reynolds stress field was performed; this analysis provides detailed information about turbulence production from various events which occur in a turbulent flow (Kim *et al.* 1987; Willmarth & Lu 1972). Fractional

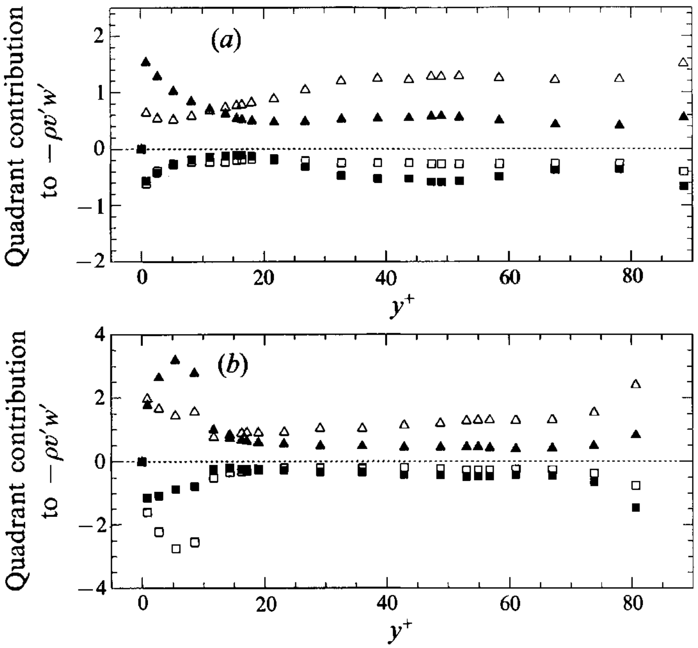

FIGURE 20. Comparison of quadrant analysis over (a) the smooth and (b) riblet walls. □, Quadrant I; △, quadrant II; ■, quadrant III; ▲, quadrant IV.

contributions to the total Reynolds shear stress $-\rho\overline{v'w'}$ were computed and analysed at each point in the domain. We adopt the standard quadrant analysis notation, see Kim *et al.* (1987): Quadrant I represents ($w' > 0$, $v' > 0$) events, quadrant II represents ($w' < 0$, $v' > 0$) events, quadrant III represents ($w' < 0$, $v' < 0$) events, and quadrant IV represents ($w' > 0$, $v' < 0$) events.

In figure 20 we examine and compare the fractional contributions from each quadrant as a function of the normal wall coordinate above the smooth and riblet walls. The quadrant analysis was performed over a time sample of roughly 250 non-dimensional time units; a spanwise location corresponding to the riblet midpoint was used for the analysis over the riblet wall. The smooth-wall results in figure 20 are in good agreement with the turbulent (smooth) channel flow quadrant analysis of Kim *et al.* (1987). We see that near the smooth wall, turbulent shear stress production is dominated by sweeping or inrushing events from quadrant IV. At $y^+ \approx 12$ there is a crossing point between quadrant IV and quadrant II contributions; above this point bursting or ejection events (quadrant II) dominate. This crossing point above the smooth wall is in good agreement with the crossover point identified from analysis of the higher-order statistics (see §4.3.5). In general, quadrants II and IV (positive production) have larger contributions to the shear stress production; the contributions of quadrants I and III are relatively small. Examination of the quadrant analysis over the riblet wall reveals some differences compared to the smooth-wall results. Away from the wall, the general distribution of the contributions from each quadrant seems to be similar to that of the smooth wall. It seems, however, that the crossover point between quadrants II and IV is shifted slightly farther away from the wall by the riblets, to $y^+ \approx 13$. In addition, in the near-wall region the contributions from quadrants I and IV are significantly increased for the riblet wall. Both of these quadrants have $w' > 0$ events in common. This finding is consistent

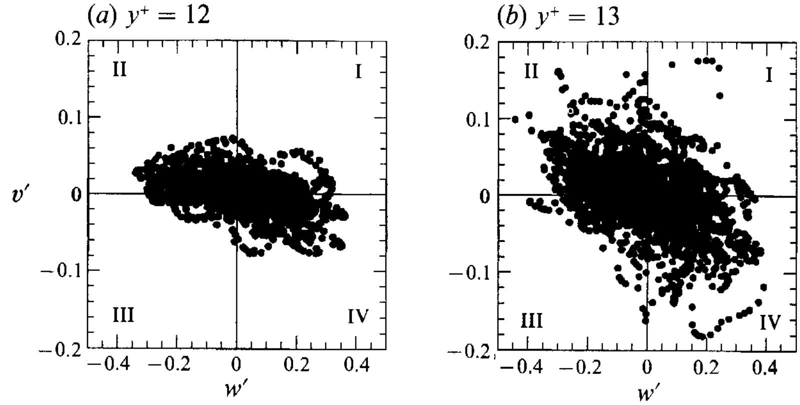

FIGURE 21. Comparison of distributions of the instantaneous quadrant contributions at (a) the smooth and (b) riblet wall crossover points.

with the examination of the higher-order moments of the streamwise velocity fluctuations (in §4.3.5), which shows large positive peaks in the skewness factors of w' within the riblet valleys.

In figure 21, we visually examine the distribution of the quadrant contributions on y-planes at a single instant in time. The instantaneous contributions from each quadrant are depicted at y-locations corresponding to the crossing points above the smooth and riblet walls. At this time instant, we see that above both walls quadrants II and IV do indeed dominate the turbulent shear stress production, and that the contributions from both of these quadrants are roughly equal (as they should be, at the crossing point). Note, however, that the contributions from the various events seem to be more evenly distributed between the quadrants above the riblet wall. Above the smooth wall the pattern of events is strongly skewed into quadrants II and IV only; above the riblet wall the pattern is much less eccentric, although the bursting and sweeping events still dominate.

4.3.4. *Temporal analysis*

A VITA analysis (Blackwelder & Kaplan 1976) was performed on the streamwise and normal velocity signals above the smooth and riblet walls. A VITA average (in this example, performed on the instantaneous streamwise velocity w) is defined as follows:

$$\hat{w}(x_i,t,T) = \frac{1}{T}\int_{t-\frac{1}{2}T}^{t+\frac{1}{2}T} w(x_i,s)\,\mathrm{d}s, \tag{13b}$$

where the VITA averaging period T should be on the order of the timescale of the phenomena under study (bursting, in this case). A localized variance may now be defined as

$$\widehat{\mathrm{var}}(x_i,t,T) = \widehat{w^2}(x_i,t,T) - [\hat{w}(x_i,t,T)]^2. \tag{13c}$$

This localized variance is a positive-definite quantity. Finally, we define a detection function as follows:

$$D(t) = \begin{cases} 1 & \text{if } \widehat{\mathrm{var}} > k w_{\mathrm{rms}}^2 \\ 0 & \text{otherwise,} \end{cases} \tag{13d}$$

where k is the threshold level used in the detection criterion. We note that

$$\bar{w}(x_i) = \lim_{T\to\infty} \hat{w}(x_i,t,T), \quad \overline{w'^2}(x_i) = \lim_{T\to\infty} \widehat{\mathrm{var}}(x_i,t,T). \tag{13e,f}$$

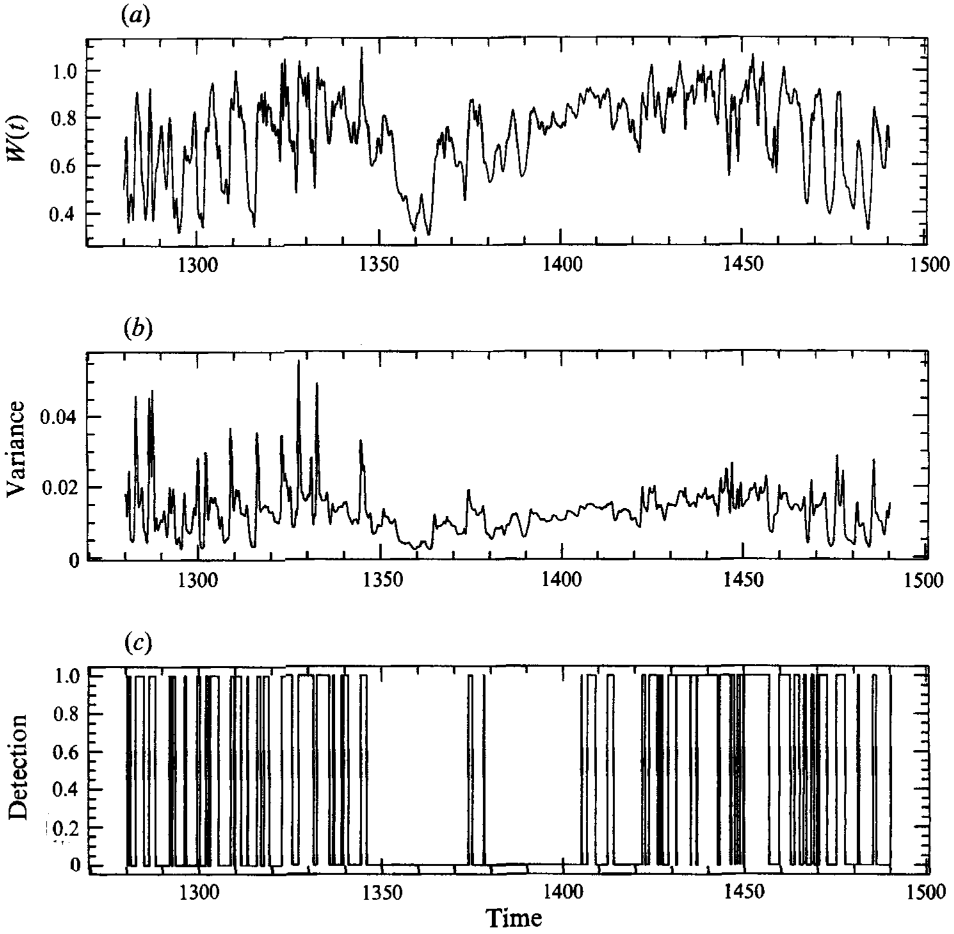

FIGURE 22. VITA analysis example showing (*a*) streamwise velocity signal, (*b*) localized variance signal, and (*c*) detection function.

Blackwelder & Kaplan (1976) suggest a VITA averaging period corresponding to $T^+ = Tu_\tau^2/\nu = 10$ and a detection threshold of $k = 1.2$ for use in burst detection; these values of T^+ and k were used in the following analyses. Figure 22 is an example of the VITA technique applied to a streamwise velocity signal obtained at a single point in the computational domain. The actual velocity signal is shown at the top, followed by its corresponding localized variance, and at the bottom, the detection function.

The VITA analysis was applied to selected points near the smooth and riblet walls (above the riblet midpoint); in figure 23 we compare the results. Here the bursting frequency is non-dimensionalized using the half-channel height δ and the centreline velocity W_c. This form of non-dimensionalization (as compared to using wall coordinates) greatly diminishes the effects of the uncertainties encountered in choosing the correct shear velocity for the riblet wall Walsh (1990*b*). According to figure 23, the peak bursting frequencies above both walls are roughly the same, but the riblet wall seems to significantly shift the location of the peak frequency farther away from the wall. When one computes the same bursting frequency profiles in wall coordinates, however, the shift of the peak location away from the wall is still present

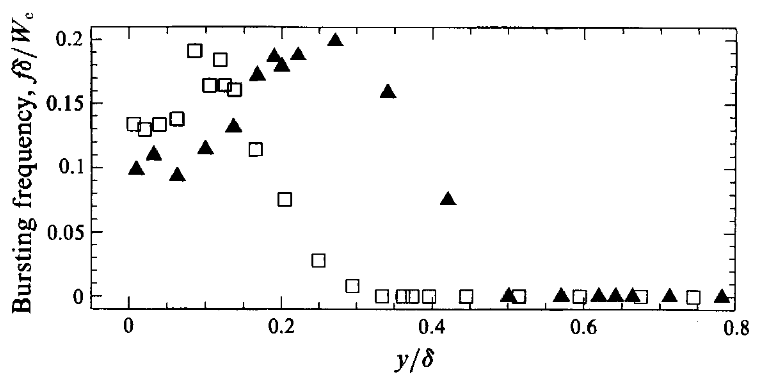

FIGURE 23. Comparison of bursting frequencies over the smooth (□) and riblet (▲) walls, as computed from the VITA analysis.

above the riblets, but it is much smaller. This is consistent with the findings of the quadrant analysis, which showed a slight upwards (away from the wall) shift of the quadrant II and IV crossover point above the riblet wall. In addition, there is a decrease in the bursting frequency very close to the riblet wall, in the valley midpoint region.

Although no change in the peak bursting frequency was detected, the results from the analysis do show a slight increase in the burst duration for the events above the riblet wall. The VITA technique was also applied to the normal velocity time signals above both walls. The only trend to emerge from these analyses was that the normal velocity fluctuations above the riblet wall had a decreased bursting frequency compared to the smooth wall.

4.3.5. *Higher-order statistics*

The third and fourth moments of the velocity fluctuations have also been computed, and are presented below. The computed values above the smooth wall are in good agreement with both experimental and other computational results (Vukoslavčević *et al.* 1987; Kim *et al.* 1987; Kreplin & Eckelmann 1979; Moin & Kim 1982).

Figures 24 (*a*, *b*), 25 (*a*, *b*), and 26 (*a*, *b*) show the skewness and flatness factors of the streamwise, normal, and spanwise velocity components, respectively, across the channel in global coordinates. In each figure, the solid line represents a profile taken from the riblet tip to the smooth wall, the dotted line corresponds to a riblet midpoint origin, and the dashed line is a profile from the riblet valley. A reference line has also been drawn in each figure, corresponding to the skewness and flatness factors of a Gaussian distribution (0 and 3, respectively). All the profiles collapse to the same results above $y \approx 0.35$; this shows the extent of the riblet wall's influence on the skewness and flatness factor profiles. It is expected that the small oscillations in the profiles will disappear if a larger time sample is taken.

Let us now consider the profiles of $S(\overline{w'})$ and $F(\overline{w'})$ in figures 24 (*a*) and 24 (*b*). Large positive skewness values indicate regions where the velocity is generally less than the mean, with occasional large excursions to values greater than the mean (Walsh 1990*b*). Large flatness values correspond to brief periods of large deviation from the mean. These types of behaviour are to be expected in the near-wall regions, where rare but large-amplitude fluctuations in w' correspond to intermittent 'sweeps' of high-momentum fluid towards the wall. The computed skewness and flatness factor

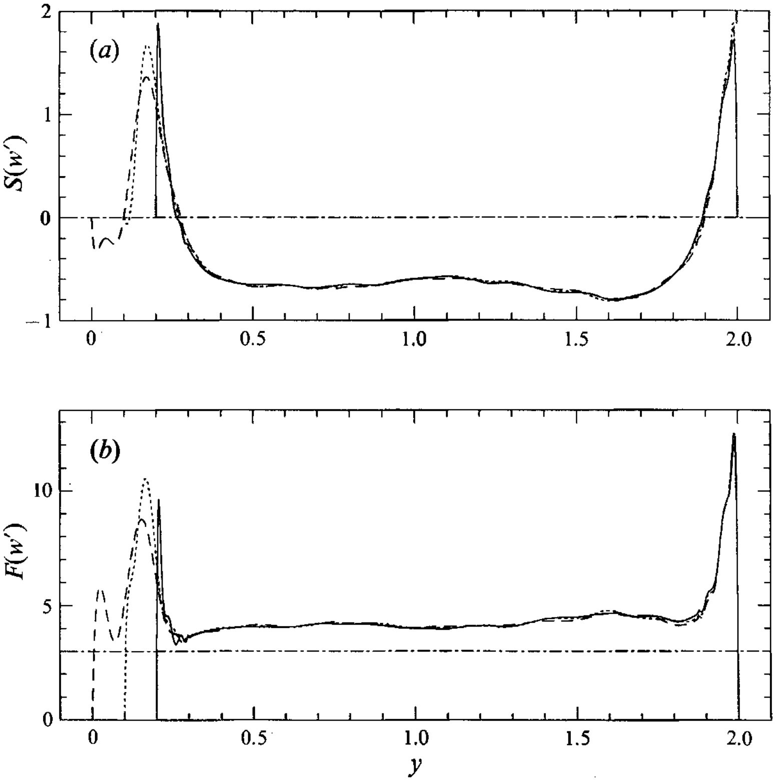

FIGURE 24. Streamwise (*a*) skewness and (*b*) flatness factor profiles across the channel, in global coordinates: ——, tip; ······, midpoint; ---, valley.

profiles reach their maxima near the walls. Comparison of the $S(w')$ profiles above both walls shows that the riblets have little effect on the streamwise skewness factor peak values in these regions; a small reduction near the riblets may occur. The peak streamwise flatness values, however, seem to be substantially reduced near the riblets, indicating reduced intermittency in the streamwise fluctuations. It is important to note that the skewness and flatness profiles above the midpoint and valley locations (dotted and dashed lines) actually peak *inside* the riblet valley regions (below $y = 0.2$), and are close to negligible below the midpoints ($y = 0.1$). This shows that occasional penetration of high-speed fluid into the riblet valleys occurs to locations as low as the midpoint (approximately); below this point the fluctuations are somewhat symmetric and relatively small. These findings are in general agreement with those of Vukoslavčević *et al.* (1987). Directly above the riblet valley, there is actually a region of negative skewness $S(w')$.

Moving away from the wall, the profile of $S(w')$ is positive, showing large excursions of $w' > 0$ (sweeps), and then becomes negative, indicating the occurrence of large excursions of negative w', corresponding to bursting activity farther away from the wall. This is consistent with findings of §4.3.3, which showed that quadrant IV events (sweeps) dominate close to the wall, and quadrant II events (bursts) dominate farther away from the wall. The $S(w')$ profile crosses zero at $y^+ \approx 12$ over the smooth wall, showing excellent agreement with the crossing point of $y^+ \approx 12$ identified from the quadrant analysis. If we now examine the skewness and flatness profiles of v' (figure 25*a, b*), we confirm that $S(v')$ also changes sign at $y^+ \approx 12$ above

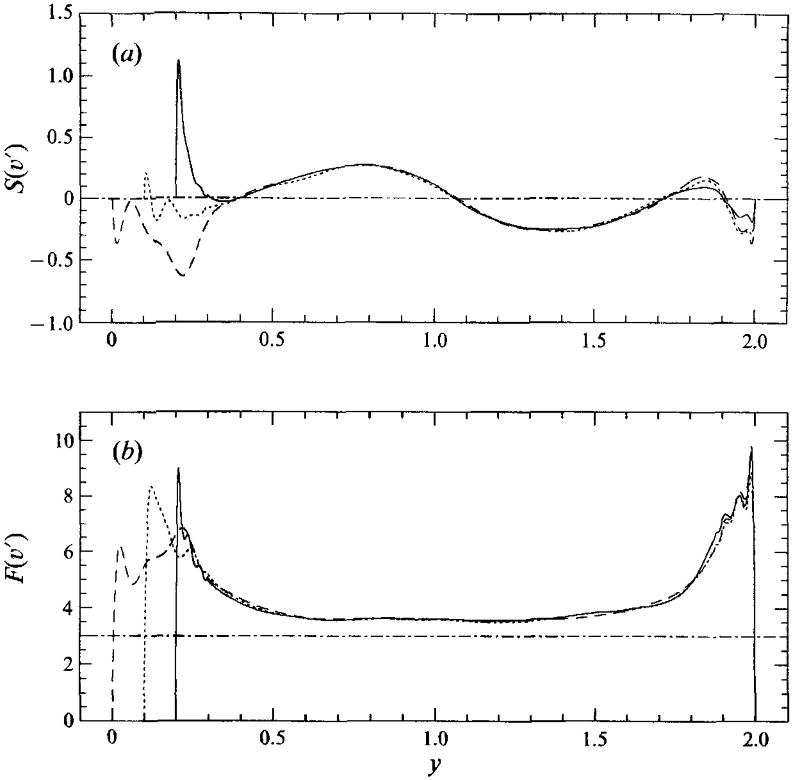

FIGURE 25. Normal (*a*) skewness and (*b*) flatness factor profiles across the channel, in global coordinates. Curves defined as in figure 24.

the smooth wall. The sign of $S(\overline{v'})$ is reversed above the smooth wall due to the direction of the normal coordinate y. As with the streamwise fluctuations, the flatness factors of the normal fluctuations seem to be slightly reduced above the riblet wall (compared to the values above the smooth wall), indicating reduced intermittency. Also note that peaks in $F(\overline{v'})$ also occur *inside* the riblet groove, and that above the riblet valley location there is a significant region of negative skewness in v'. It is interesting to note that there is a large-amplitude positive peak in $S(\overline{v'})$ directly above the riblet tip. This large positive skewness identifies the riblet tip as a region where large excursions to values greater than the mean occur in the normal velocity component.

Figure 26 (*a*, *b*) shows the skewness and flatness factors of the spanwise fluctuations u'. The skewness profiles are basically zero across most of the channel; the non-zero values near the centreline are due to the short time sample length. The riblet walls have little effect on $S(\overline{u'})$ away from the riblets. Very near the riblets, however, there seems to be some activity in the spanwise velocity fluctuations. There are regions of non-zero skewness of u' for $y < 0.25$; recall the slight bump in the u_{rms} profile in figure 14, suggesting spanwise motions even deep within the riblet grooves. Further insight into this phenomenon will be given in §4.4. The flatness factor profiles $F(\overline{u'})$ show large increases in peak values near the riblets, suggesting that large spanwise fluctuations are much more intermittent near the riblet wall, compared to the small wall. This effect has also been reported in the experimental data of Wallace & Balint (1987), and Hooshmand (1985). Walsh (1990*b*) notes that this u' dampening is

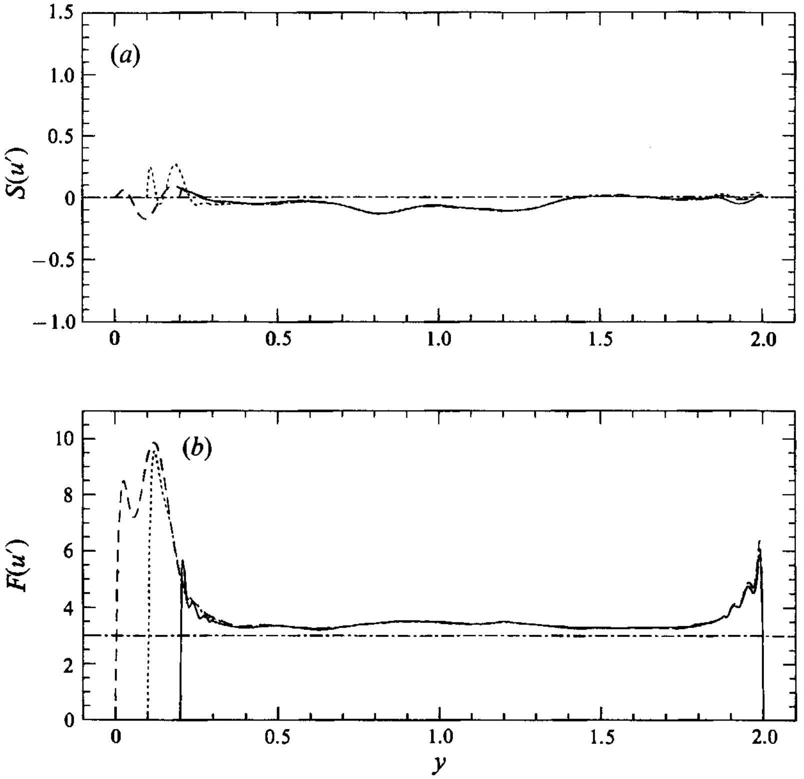

FIGURE 26. Spanwise (*a*) skewness and (*b*) flatness factor profiles across the channel, in global coordinates. Curves defined as in figure 24.

consistent with the hypothesis that the spanwise motion of low-speed streaks is reduced by the presence of the riblets.

4.4. *Turbulent flow structure and physics*

In this section, we now turn our attention to the instantaneous flow field, and the turbulent flow structures it contains. As mentioned in §3.1, our use of a channel with both smooth and riblet-mounted walls allows the simultaneous comparison of flow field structures in the boundary layers near both walls. A qualitative investigation of the turbulent flow structure in the riblet channel will be carried out, using flow visualization results presented with colour contour plots. Once again, we examine results from $Re = 3500$; the flow visualization pictures correspond to the same single time instant, taken well after a turbulent stationary state has been reached. The instantaneous velocity, vorticity, and Reynolds stress component $-\rho v'w'$ fields are examined at various locations in the computational domain.

4.4.1. *Instantaneous plane contours*

Insight into the nature of the various structures present in the flow field can be gained by viewing flow contours on different planes at the same time instant. Examination of contours on spanwise (constant-x) slices throughout the domain revealed the existence of large-scale streaky structures near both top and bottom walls. From the velocity contours it was seen that regions corresponding to low-momentum fluid had ejection-type motions (normal velocities away from the wall)

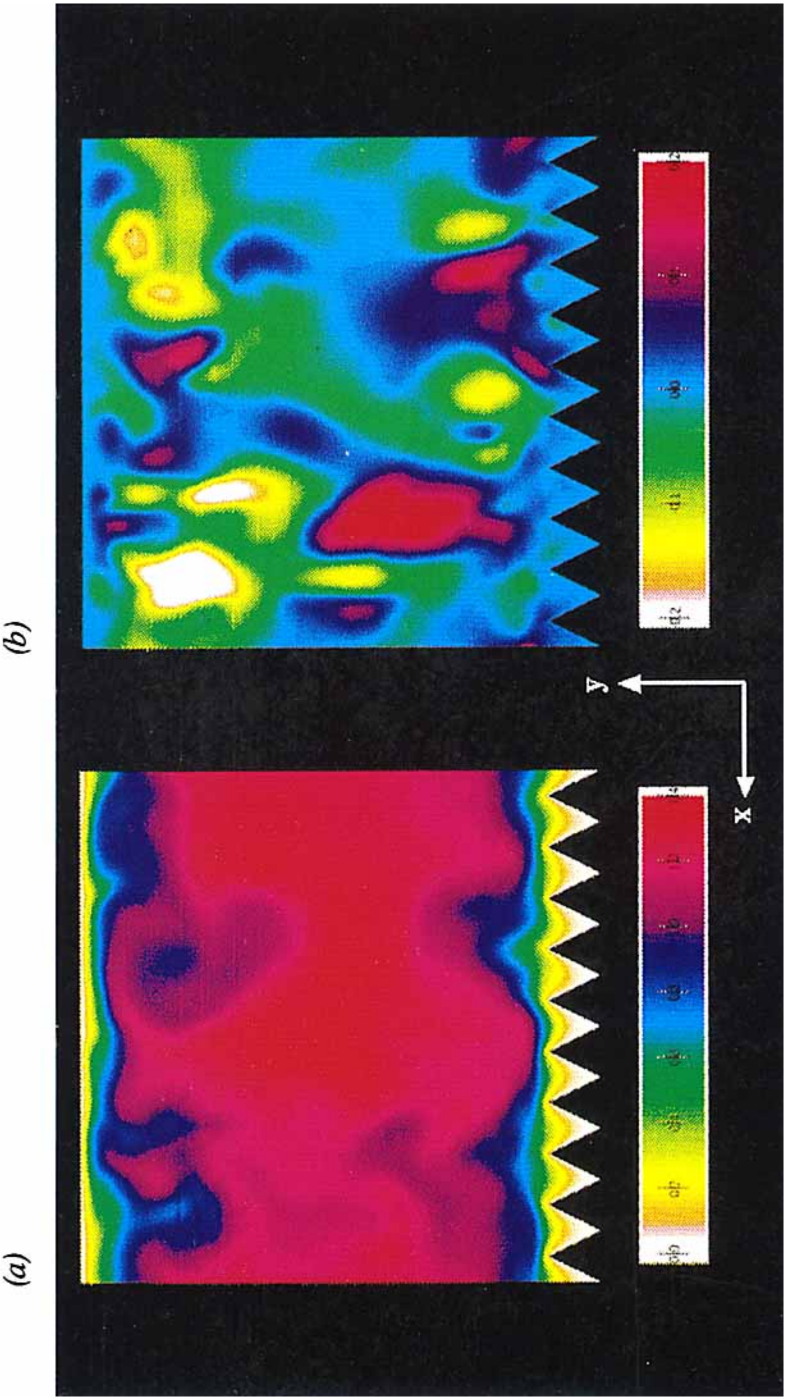

FIGURE 27. (*a*) Instantaneous streamwise (*W*) and (*b*) normal (*V*) velocity contours on a z-plane (z=0, $x \in [0, 2.0]$, $y \in [0, 2.0]$). Flow is into the page.

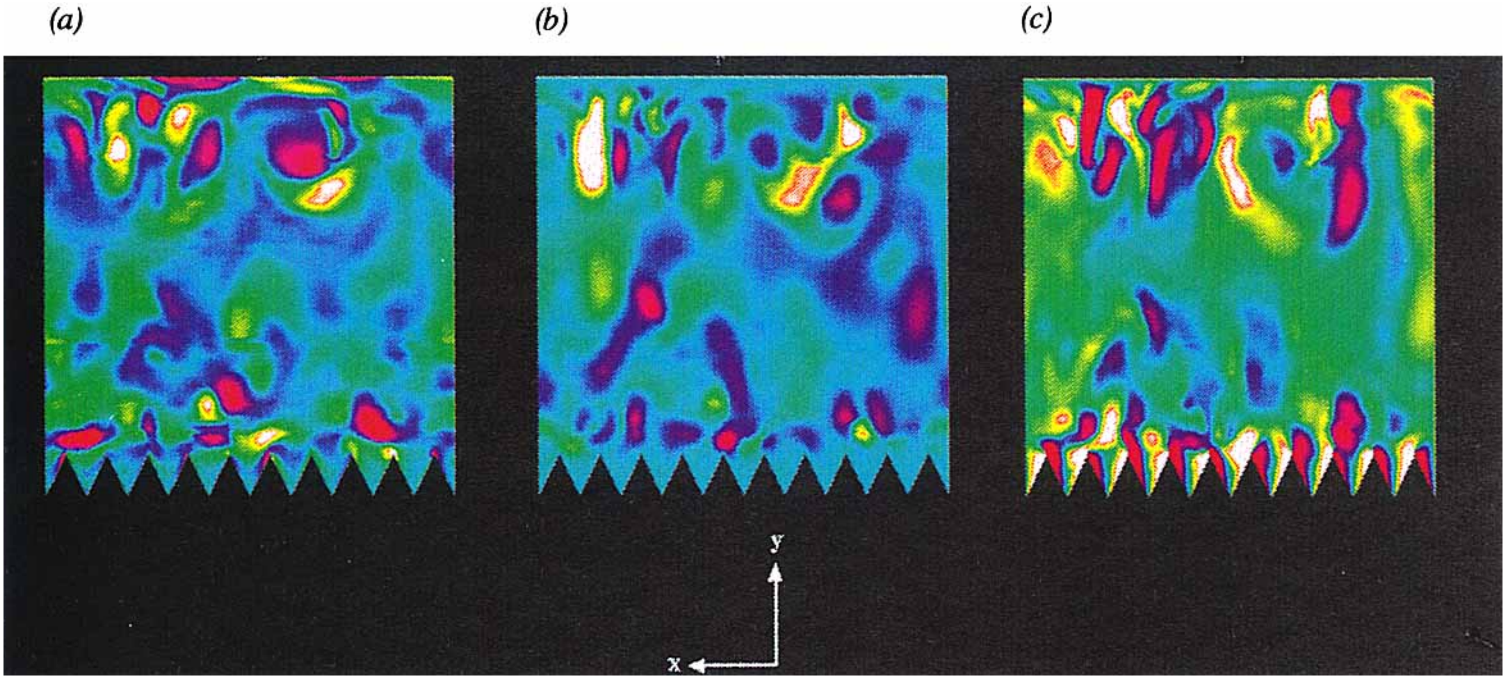

FIGURE 28. *(a)* Instantaneous streamwise vorticity (ω_z), *(b)* $-\rho v'w'$, and *(c)* normal vorticity (ω_y) contours on a z-plane (z=0, $x \in [0, 2.0]$, $y \in [0, 2.0]$). Flow is into the page.

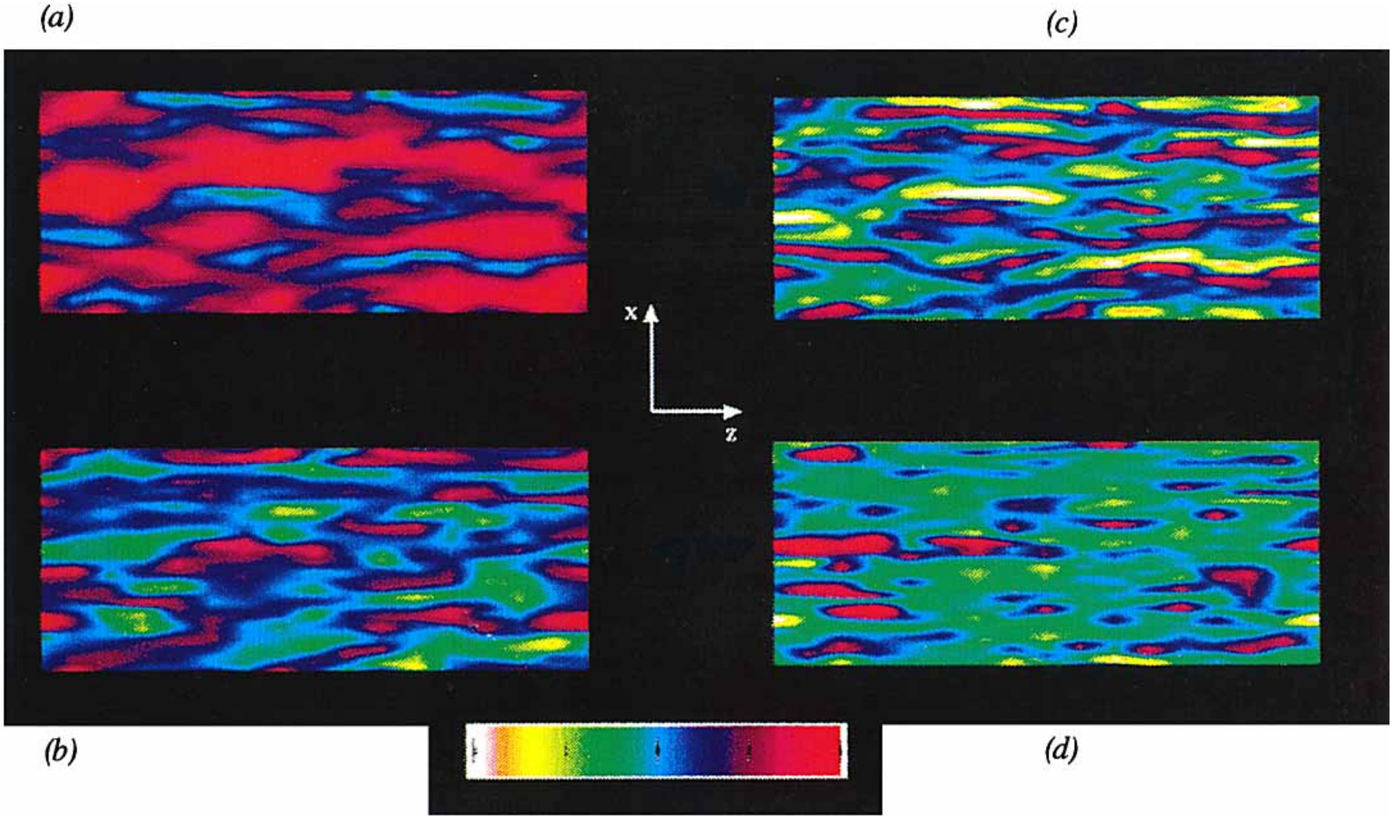

FIGURE 29. *(a)* Instantaneous streamwise *(W)* and *(b)* normal *(V)* velocity, *(c)* normal vorticity (ω_y), and *(d)* $-\rho v'w'$ contours on a y-plane near the riblet wall ($y^+_{\text{riblet}} = 13$, $x \in [0, 2.0]$, $z \in [0, 5.0]$). Flow is from left to right.

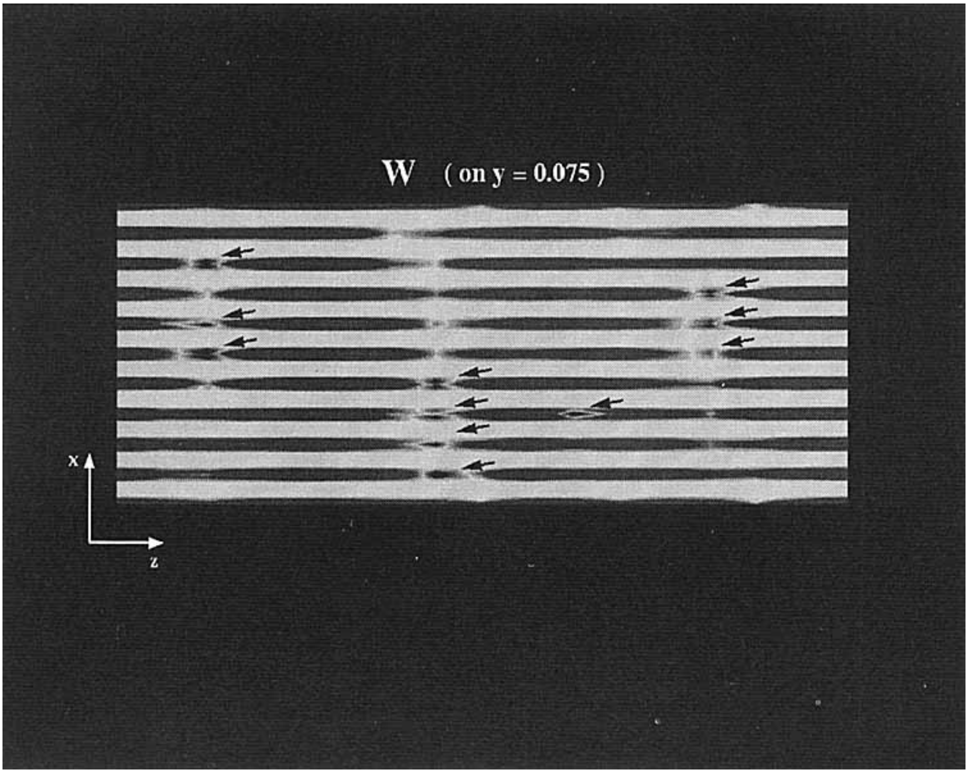

FIGURE 30. Instantaneous streamwise velocity contours on the plane $y = 0.075$ showing flow reversal (arrows) deep within the riblet valleys.

associated with them and regions of high-speed fluid had strong inrush-type motions associated with them. The vorticity and instantaneous Reynolds stress contours revealed that there was a high correlation between the aforementioned bursting and sweeping events, concentrations of positive and negative vorticity, and positive stress production (regions of negative Reynolds stress).

We now examine instantaneous contours on a typical streamwise slice. The plane we consider is located at $z = 0.25$, corresponding to $(x \in [0, 2.0], y \in [0, 2.0])$ in the computational domain. Note that the riblets are symmetrical triangles with height and base $h = s = 0.2$. The flow direction for these streamwise plane figures is into the page.

Figure 27 (plate 1) depicts instantaneous streamwise velocity contours on this z-plane (figure 27*a*); the colour scale ranges from $W = -0.027$ (white) to $W = 1.38$ (red). At $x \approx 0.6$ (just right of centre), we see the large eddy-like structure of a faint low-speed region which extends quite some distance from the top wall to $y \approx 1.65$. Note also the mushroom-shaped low-speed structures near the top wall in the upper left corner, and the structures near the lower wall at $x \approx 0.7$ and $x \approx 1.7$; all of these regions correspond to long streak-like structures in the spanwise-plane contour plots. It will become apparent, as we view contours of the normal velocity, vorticity, and $-\rho v'w'$, that we are viewing low-speed streak-like structures (and their associated high-speed sweeps events) in various stages of the bursting process.

Figure 27 (*b*) shows the instantaneous normal velocities on the same plane. In this picture, white/yellow represents negative normal velocities (downwards motion), and red/purple represents positive normal velocities (upwards motion); the colour scale ranges from $V = -0.2$ to $V = 0.2$. It is immediately obvious that the low-speed structures in the W contour plot have violent ejection motions (away from the wall) associated with them. Furthermore, it is interesting to note that, in general, these regions are immediately adjacent to areas of inrushing high-speed fluid. For example, two sweep events at $x \approx 0.35$ and $x \approx 1.0$ (white regions on the V plot) surround the lower wall burst at $x \approx 0.7$. The large eddy-like structure pointed out earlier at ($x \approx 0.6$, $y \approx 1.65$) seems to be the end of an ejection event; a streak has lifted away from the upper wall (its remnant is still visible at $x \approx 0.4$, $y \approx 1.9$), and this blob has broken off from it and has been convected in the positive x-direction, its negative normal velocity greatly diminished at this time.

In figure 28(*a*) (plate 2) (far left picture), contours of the instantaneous streamwise vorticity are shown. In this plot, white/yellow represents negative ω_z and red/purple represents positive ω_z. From these contours, we now see that the bursting and sweeping events identified in figure 27 are actually related to both pairs of counter-rotating vortices and single isolated vortices. The mushroom-shaped streaks in the upper left corner of the W plot have counter-rotating vortices on either side of them, with negative normal velocity regions occurring in the centre of each pair. This phenomenon is consistent with the widely accepted model of pairs of counter-rotating vortices (which form hairpin vortices) lifting streaks of low-speed fluid away from the wall (giving rise to ejection events) and sweeping high-momentum fluid down to the wall in regions surrounding the burst (Robinson 1989; Wallace 1982; Smith *et al.* 1989). Note also that the detached eddy discussed before (at $x \approx 0.6$, $y \approx 1.65$) also has a pair of counter-rotating vortices associated with it; they seem to have been similarly stretched/convected in the positive x-direction. The event at $x \approx 1.7$ near the riblet wall seems to be at a much later time in the bursting process; a pair of weaker counter-rotating vortices can still be distinguished near the wall in that region (see bottom left region figure 28*a*).

The $-\rho v'w'$ contours on this plane are depicted in figure 28(*b*) (plate 2). Positive turbulent shear stress production (negative Reynolds stress) is represented by red/purple in the lower half of the channel (near the riblet wall) and by white/yellow in the upper (near the smooth wall). This difference in colour is because the sense of the normal coordinate is reversed in the upper half of the channel (negative V represents movement away from the upper wall). We see that the areas of positive turbulent stress production coincide closely with the burst and sweep events. We note that there is a high concentration of $-\rho v'w'$ at $x \approx 1.1$, $y \approx 0.25$, although no clear structure seems to be apparent there in the W plot of figure 27. Further examination of the z-plane V and ω_z contours, however, show that an inrush event seems to have occurred there; there are also pairs of counter-rotating vortices in existence at this location.

Finally, we examine the instantaneous ω_y contours in figure 28(*c*) (plate 2). Again, in this figure white/yellow represents negative y-vorticity and red/purple represents positive y-vorticity. We see the presence of the low- and high-speed streak-like regions (more detailed views can be obtained on the x- and y-planes), and the extent to which they reach away from the walls. It seems that the presence of the riblets are giving rise to secondary vortices inside the riblet valleys, perhaps a phenomenon similar to the flow in the corners of a square duct (i.e. shear-driven secondary flow inside the riblet grooves). When viewing the ω_z contours, selectively changing the colour contour threshold also shows positive and negative regions inside the riblet valley. Recall the existence of non-zero $S(u')$ and $S(v')$ skewness factors deep inside the valleys (figures 25, 26), the slight bump in the u_{rms} profile (figure 14) taken through the riblet valley, and the large peaks in $S(v')$ near the riblet tips (figure 25*a*). It has been suggested by Bechert & Bartenwerfer (1989), Bacher & Smith (1985), Choi (1989), and Luchini, Manzo & Pozzi (1991) that the riblets interfere with (dampen) the secondary cross-flow associated with the longitudinal vortices present in the flat-plate boundary layer, and therefore manage to reduce the relative turbulence level and produce secondary vortical motions.

We now view instantaneous contours on a typical normal plane, located at $y^+ \approx 12$ above the riblet wall (the crossing point identified from the quadrant analysis performed in §4.3.3). This plane corresponds to $(x \in [0, 2.0], z \in [0, 5.0])$ in the computational domain, and the flow is from left to right.

Figures 29(*a*) and 29(*b*) (plate 3) show the instantaneous streamwise and normal velocities on the y-plane near the riblet wall. Colours are the same as in the velocity plots of figure 27; in the V plot, white/yellow represents negative or downwards normal velocities and red/purple represents positive or upwards normal velocities. Once again, we see that the long streak-like low-speed regions are highly correlated with normal velocity contours indicating motions away from the walls, and that there are corresponding inrushes of high-momentum fluid towards the walls.

The top right and bottom right plots of figures 29(*c*) and 29(*d*) (plate 3) show the instantaneous normal vorticity and Reynolds stress on the y-plane near the riblet wall. The large spanwise variation in positive and negative ω_y concentrations is caused by the presence of elongated regions of high- and low-momentum fluid immediately adjacent to each other. Note that the locations of the streaks in the W plot are very accurately predicted by the existence of pairs of streak-like positive and negative ω_y contours. As before, we see from the instantaneous Reynolds stress contours (colours are as in the $-\rho v'w'$ plot of figure 28) that positive production is highly correlated with the quadrant II and IV (burst and sweep) events.

Only general, qualitative comparisons can be made between the smooth-wall events and the riblet-wall events by using these instantaneous 'snapshots'. Flow visualization movies have been made to assist us in making some empirical observations; these movies allow us to compare the smooth-wall and riblet-wall flow structures as they evolve in space and time. Time evolution of contours on z-planes showed that the average streak spacing in both cases was on the order of $\lambda \approx 90$ wall units. The riblet-wall streak spacing seemed to be slightly larger than that of the smooth wall, but this result is strictly qualitative, as it was obtained through flow visualization techniques. It was seen from time evolution of contours on y-planes that the average 'thickness' or size of the low-speed streaks was smaller near the riblet wall. While the actual number and frequency of positive shear stress production events (identified from the $-\rho v'w'$ contours) near the smooth and riblet walls were similar, increasing the threshold levels on the colour contours showed that the magnitudes of the events above the smooth wall were consistently higher than those of the riblet wall. This was an expected result, considering the larger peaks above the smooth wall in the time-averaged Reynolds stress profiles (see figure 18).

The spanwise motion of the streak-like structures was much more oscillatory (wavy) above the smooth wall; the streaks above the riblet wall appeared to be more strongly anchored in their spanwise locations, presumably due to the presence of the riblet geometry below. This inhibition of the lateral movement of the wall streaks near the riblets is consistent with the increased flatness factors $F(u')$ reported near the riblet wall in §4.3.5. Further discussion of this phenomenon will proceed in §4.5.

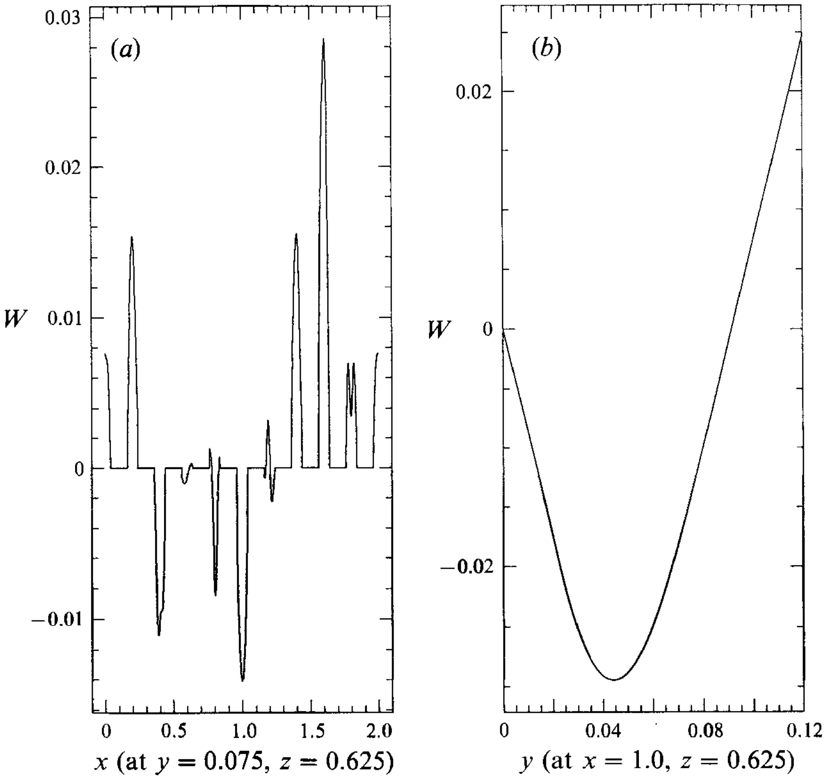

FIGURE 31. (*a*) Instantaneous W-profiles within the riblet valley along the span of the domain from $(0, 0.075, 0.625)$ to $(2.0, 0.075, 0.625)$ and (*b*) detail of flow reversal region from $(1.0, 0, 0.625)$ to $(1.0, 0.12, 0.625)$.

4.4.2. *Flow reversal*

While from the contour plots in the preceding sections it is apparent that the velocities inside the riblet valleys are small, they are not completely non-negative. In §4.3.5, analysis of the higher-order turbulence statistics showed that strong sweeping events penetrated to regions deep within the riblet valleys. These inrushes of high-speed fluid have been observed to impinge on the wall surface and result in what has been described as 'the splatting effect' by Moin & Kim (1982). It is therefore not surprising to observe instantaneous flow reversal even in regions deep within the riblet valleys.

Figure 30 is a greyscale plot of instantaneous streamwise velocity contours taken at an instant in time on the plane $y = 0.075$. This plane, which is defined by $(x \in [0, 2.0], z \in [0, 5.0])$, passes through the riblet valleys at a location just below the midpoint $y = 0.1$. In this plot, the W-scale ranges from $W = -0.015$ to $W = 0.015$; white corresponds to zero-velocity regions (including those points that fall inside the riblet wall), and the grey shades represent positive streamwise velocity regions. The darkest regions (identified by the arrows) are areas of reverse flow $W < 0$. We see that at this time instant, there are several areas of negative streamwise velocity inside the riblet valleys. On this y-plane, three large regions of reverse flow can be easily distinguished, along with a smaller area at $(z \approx 3.2, x \approx 0.8)$.

We now proceed to examine one of these flow reversal regions in more detail. Figure 31 (*a*) is a profile of the instantaneous streamwise velocity plotted along the span of the domain on the line $y = 0.075$, $z = 0.625$, $x \in [0, 2.0]$; this corresponds to

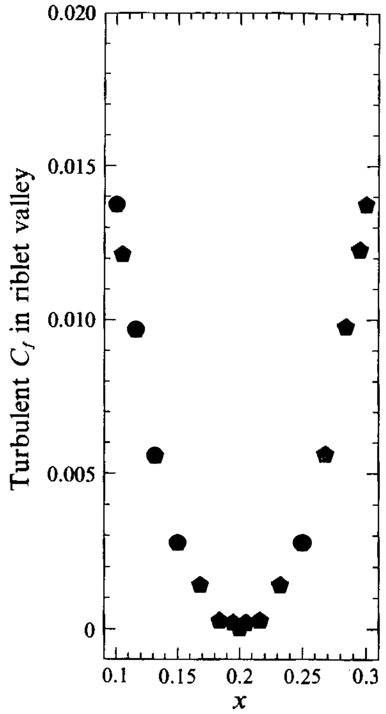

FIGURE 32. Turbulent local skin friction distribution inside triangular riblet valley ($Re = 3500$).

a line passing through the flow reversal regions depicted in the upper left corner of figure 30. We see that these flow reversal regions are not negligible, the area at $x = 1.0$ reaching a negative velocity of $W \approx -0.014$ on this plane. In figure 31(*b*), we examine this particular valley in finer detail; W is plotted along the normal direction on the line $x = 1.0$, $z = 0.625$, $y \in [0, 0.12]$ (at the valley trough). There is a considerable region of reverse flow deep within the valley, and at this point the flow reversal reaches a magnitude on the order of 2.5% of the bulk streamwise velocity. This particular negative-W region extends all the way up to just below the midpoint of the valley ($y = 0.1$) at this time instant. Our findings of flow reversal regions even deep within the riblet valleys serve to further confirm the necessity of using Navier–Stokes computations (instead of simplified models) to investigate the turbulent flow of riblets.

4.5. *Drag reduction*

In §4.1, the distribution of the local skin friction inside the riblet valley in the laminar flow regime was examined (see figure 9). We now compare this result to the local C_f distribution inside the riblet valley in the turbulent regime, at $Re = 3500$. Figure 32 shows values of the local skin friction at collocation points along the riblet valley wall at this Reynolds number. The riblet wall has a lower average C_f than the smooth wall. We note that the shapes of the C_f distributions (higher at the peaks, lower at valleys), are identical for the laminar and turbulent cases. The drag results, however, are different. As was mentioned in §4.1, the riblet wall had a drag penalty at $Re = 1000$. In the $Re = 3500$ case, the riblet wall has a lower drag than the smooth wall, despite the wetted area increase. At this Reynolds number, a 6% drag reduction is realized.

These drag calculations were made by computing directly the viscous stress tensor

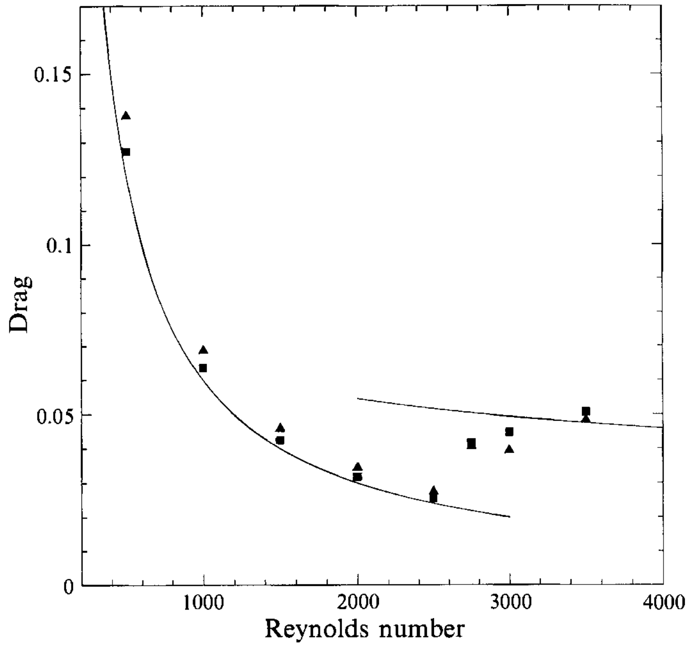

FIGURE 33. Drag on each wall *vs.* Reynolds number for riblet channel simulation: ——, smooth channel result; ■, flat wall; ▲, riblet wall.

on both walls and checking these values via a global momentum balance using the pressure drop from equation (7) in §2.1. In figure 33, we present the drag results at various Reynolds numbers in the laminar, transitional, and turbulent flow regimes. These computations were performed on the M2 mesh described in §3.1; we believe that they are more accurate than preliminary numbers published earlier (Chu & Karniadakis 1991; Chu *et al.* 1992). The squares represent the overall drag on the upper smooth wall, and the triangles correspond to the overall drag on the lower riblet wall. The solid line in the figure correspond to the exact laminar solution and an empirical data fit (Dean 1978) for a channel with two smooth walls; these are included for reference purposes only. Compared to the smooth wall, the riblet wall always has a higher drag in the laminar regime. This trend reverses in the transitional and turbulent regimes; it appears that a drag reduction of approximately 6% exists for the riblet wall at Reynolds number 3500. The results at $Re = 3000$ show a larger drag reduction, but the sample size at this Reynolds number (which appears to be in the transition regime) was only a fraction of the sample taken at $Re = 3500$; while the $Re = 3000$ drag result shows the correct trend, a longer time sample is needed to verify the exact values.

In §4.4.1 it was noted qualitatively that the average streak spacing for the riblet wall (at $Re = 3500$) seemed to be slightly larger than the corresponding value for the smooth wall. This would correspond to a relative reduction in bursting activity for the same time cycle taken over both walls. Since the eruption process is directly proportional to the level of momentum exchange at the wall, this is consistent with the reduced levels of drag at the riblet wall.

The wall streaks near the riblet wall appeared to be more firmly anchored at their spanwise stations. We recall from §4.4.1 and figure 28 that there seem to be some important vortical structures and corresponding secondary flow inside the riblet

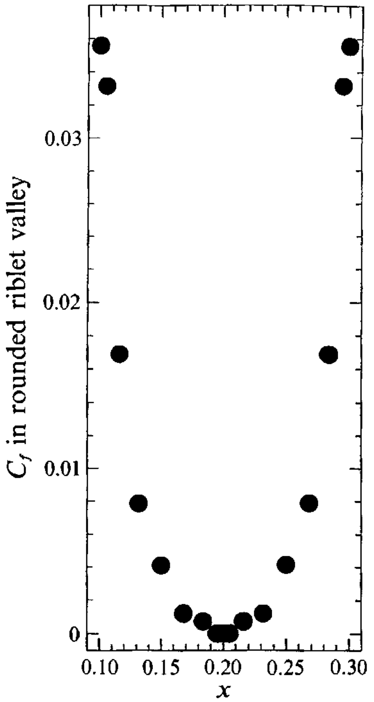

FIGURE 34. Local skin friction distribution inside rounded riblet valley at $Re = 1000$.

valleys; these are likely to be directly related to the cause of the turbulence level reductions reported above the riblet wall. In the streamwise colour contour plots, many pairs of counter-rotating vortices were seen in regions corresponding to ejection and sweeping activity; these are consistent with the bursting process model involving hairpin vortices. The riblets seem to interfere with the lateral movement of low-momentum fluid near the wall surface; it has been hypothesized that this makes the adverse pressure gradients induced by the convecting hairpin vortices less effective in provoking violent ejections from the flow regions near the wall (Smith *et al.* 1989). Thus, this inhibition of the cyclical momentum exchange between the wall and the outer flow region causes a reduction in streak formation and subsequent reductions in bursting activity and wall shear stress. Our results seem to be consistent with the riblet drag-reduction mechanism supported by Beckert & Bartenwerfer (1989), Bacher & Smith (1985), Choi (1989), Smith *et al.* (1989), and Luchini *et al.* (1991).

4.6. *Rounded riblets*

As mentioned in §3.1, some preliminary results have been obtained for the flow over rounded riblets. Experimental results reported in Walsh (1990*a*), and Walsh & Lindermann (1984) have shown that even slightly rounded riblet peaks result in decreased levels of drag reduction performance. This is an important issue, especially when one considers the practical applications of riblets, e.g. for use in the aircraft industry (Lynch & Klinge 1991). Even if it were possible to precisely machine the original riblet surface to assure sharp peaks, the tips of riblets mounted on an aircraft fusalage or wing can be expected to undergo deterioration as often as every flight operation. Therefore, it is of great interest to investigate the flow over rounded riblets. The dimensions of the rounded riblet domain are given in §3.1.

Investigation of rounded riblets in the laminar flow regime has been completed. As with the laminar results of the triangular riblet, profiles of the streamwise velocity are inflexional inside the riblet valleys. Figure 34 shows the local skin friction distribution inside the rounded riblet valley at $Re = 1000$; the circles are values of C_f at the collocation points along the rounded riblet valley. The rounded riblets have a higher average shear stress than the triangular riblets (and thus the rounded riblet wall also has a higher drag than the smooth wall) – this holds for the entire laminar regime. Similar to the triangular riblet case, there is a linear equation governing the rounded-riblet skin friction in the laminar flow regime.

Preliminary computations in the turbulent regime show that rounded riblets do not result in the reductions in turbulence intensities and Reynolds stress obtained with the triangular riblets. In fact, for the rounded-riblet dimensions presented above, it is possible that a drag increase for the riblet wall is present at $Re = 3500$. Longer time samples are needed to clarify this issue. Ongoing research also involves the investigations of the flow over other riblet shapes, in addition to the triangular and rounded riblets already described.

5. Summary and discussion

The three-dimensional incompressible Navier–Stokes equations were integrated via a spectral element–Fourier method to compute the flow in a channel with a smooth upper wall and a riblet-mounted lower wall. The objective was to investigate in detail the flow over riblets using a direct numerical simulation. Both laminar and turbulent regimes were explored in an attempt to provide detailed numerical data regarding the flow over riblets, to complement and extend the existing experimental results. We also sought to provide a database for use in future validation of turbulence modelling and new experimental techniques, such as the nine-sensor velocity–vorticity probe of Vukoslavčević, Wallace & Balint (1991) and PIV particle imaging techniques. We now present a brief summary of our results.

After briefly outlining the mathematical formulation of the governing equations in the context of the spectral element method, the convergence properties of the method were examined. Exponential convergence was demonstrated for our flow solvers, and code validation results were presented. The computational domain used in the simulations was examined, and different mesh discretizations were compared to verify the choice of the resolution employed. Steady-state solutions for the entire laminar regime were computed and discussed; it was shown that the velocity profile in the channel was inflexional inside the riblet valleys. Higher drag for the riblet wall was computed in the entire laminar regime, and the local distribution of skin friction inside the riblet valley was examined. An empirical average skin friction law was suggested for the triangular-riblet surface of the channel. The numerical procedures involving the transition to turbulence were discussed; a laminar steady-state solution was perturbed and exponential growth resulted. This flow was then integrated through transition until a stationary turbulent state was reached. Stability studies for the flow over riblets and a more thorough investigation of the transitional regime were identified as important topics for future research.

The low Reynolds number turbulent regime was investigated; a complete set of results was presented for a representative Reynolds number of $Re = 3500$. Similar to the laminar solutions, the turbulent mean velocity profile was also found to be inflexional in the riblet valleys; excellent agreement was obtained between the computed smooth-wall profile in wall coordinates and the suggested 'law of the wall' relations. Various bulk flow properties were computed, and a comparison between the riblet wall and smooth wall was made, indicating consistency with the computed velocity profiles and drag reductions. Flow reversal was found to occur even in regions deep within the riblet valleys; this, along with our findings of turbulence intensity activity and peaks in the higher-order moments inside the riblet valleys, demonstrates the necessity of performing full Navier–Stokes simulations for turbulent flow over riblets.

A full set of turbulence statistics was computed and presented for the representative case $Re = 3500$. In all cases good agreement between the computed smooth-wall values and other turbulent channel flow computational and experimental results exists. Two-point correlations validated the size of the computational domain. Profiles of the r.m.s. velocities and Reynolds stress across the channel revealed that the riblets suppress all three components of the turbulence intensities (even at locations near the riblet tips), and result in significant Reynolds stress reductions. A quadrant analysis of the Reynolds stress field showed that the riblets shift the quadrant II and IV crossover point slightly farther away from the wall, and that there are increased contributions from quadrant I and IV events very near the riblet wall. Temporal analyses were performed, including the use of the VITA technique for burst detection. It was found that a slight shift away from the wall occurred for the peak bursting location above the riblet wall, and that on average, the ejection events may have had a longer duration above the riblet wall. No change in the bursting frequency was detected from the VITA results. These temporal results, however, are preliminary; further investigation in this area is required. Examination of the higher-order statistics demonstrated that high stress production events penetrated to locations even deep within the riblet valleys. Large values of $S(v')$ were detected near the riblet tips, and increased intermittency was seen in the spanwise fluctuations near the riblet wall. These results are consistent with the activity seen in the instantaneous flow field examinations.

The instantaneous flow field structure was examined by viewing the velocity, vorticity, and instantaneous Reynolds stress $-\rho v'w'$ fields throughout the domain at selected instants in time; flow visualization movies were also used to investigate the time evolution of the organized structures in the flow. It was seen that the boundary layers near both smooth and riblet walls consisted of low-speed streak-like structures with associated ejection motions. Corresponding inrushing regions of high-speed fluid were observed. Together with different views showing the existence of counter-rotating streamwise vortices and other vortical structures in these areas and views of $-\rho v'w'$ contours, it was seen that these bursting and sweeping events were the primary activities responsible for positive turbulent stress production.

All these findings, which were obtained using qualitative flow visualization methods, are consistent with the widely accepted model of longitudinally oriented vortices or hairpin vortex structures in the wall layers that produce the ejection and sweep events that effect turbulent momentum transfer (Robinson 1989; Wallace 1982; Smith *et al.* 1989). Further comparison between the riblet-wall and smooth-wall events revealed some interesting differences. Basically, the presence of the riblets seems to inhibit the spanwise motions of the wall streaks (consistent with the increased intermittency results of the higher-order statistics examination); the lateral resistance offered by the riblets produces secondary flow and vortical structures in the riblet valleys which were clearly detected in the vorticity examinations. It has been hypothesized that the inhibition of the spanwise motions of the low-speed fluid in the riblet-wall region results in a decrease in the 'effectiveness' of the ejection events, see Bechert & Bartenwerfer (1989), Bacher & Smith (1985), Choi (1989), Smith *et al.* (1989), Luchini *et al.* (1991), thus leading to the reductions in Reynolds stress and drag that were obtained; all of our computed results are consistent with this drag reduction mechanism.

Drag reduction for the riblet wall was reported in the transitional and turbulent regimes. At $Re = 3500$, the drag reduction was on the order of 6%. It was seen that, in the turbulent regime, the local skin friction distribution inside the riblet valley had the same general profile as in the laminar regime. Finally, results involving rounded riblets were presented.

Various issues still remain open, and ongoing research addresses such topics as: stability and transition studies, more detailed temporal analyses, non-triangular riblets, more quantitative analyses of the turbulent flow structures and the effects of the riblets upon them, and extension to higher Reynolds number regimes.

This work was supported by the National Science Foundation grant CTS-8914422, and under the contract F49620-91-C-0059 of the Defense Advanced Research Projects Agency and the Air Force Office of Scientific Research. We are grateful to Professors S. A. Orszag and G. L. Brown for all the useful suggestions and advice. We would also like to acknowledge R. Henderson and C. Crawford for their assistance.

REFERENCES

ANTONIA, R. A., TEITEL, M., KIM, J. & BROWNE, L. W. B. 1992 Low-Reynolds-number effects in a fully developed turbulent channel flow. *J. Fluid Mech.* **236**, 579–605.

BABUSKA, I. & SURI, M. 1987 The h–p version of the finite element method with quasi-uniform meshes. *Mathematical Modelling and Numerical Analysis* **21**, 199.

BACHER, E. V. & SMITH, C. R. 1985 A combined visualization–anemometry study of the turbulent drag reducing mechanisms of triangular micro-groove surface modifications. *AIAA*-85-0548.

BECHERT, D. W. & BARTENWERFER, M. 1989 The viscous flow on surfaces with longitudinal ribs. *J. Fluid Mech.* **206**, 105–129.

BECHERT, D. W., BARTENWERFER, M. & HOPPE, G. 1986 Drag reduction mechanisms derived from shark skin. In *15th Congress, Intl Council for Aeronautical Sci., London, Paper* 86-1.8.3, pp. 1044–1067.

BENHALILOU, M., ANSELMET, F., LIANDRAT, J. & FULACHER, L. 1991 Experimental and numerical investigation of a turbulent boundary layer over riblets. In *Proc. 8th Symp. Turbulent Shear Flows, Munich*, pp. 18–5,

BLACKWELDER, R. F. & KAPLAN, R. E. 1976 On the wall structure of the turbulent boundary layer. *J. Fluid Mech.* **76**, 89–112.

BUSHNELL, D. M. & HEFNER, J. N. (ed.) 1990 *Viscous drag reduction in Boundary Layers.* Progress in Astronautics and Aeronautics, vol. 123.

BUSHNELL, D. M. & MOORE, K. J. 1991 Drag reduction in nature. *Ann. Rev. Fluid Mech.* **23**, 65–79.

CHOI, H., MOIN, P. & KIM, J. 1991 On the effect of riblets in fully developed laminar channel flows. *Phys. Fluids* A **3**, 1892–1896.

CHOI, K. S. 1989 Drag reduction mechanisms and near wall turbulence structure with riblets. In *Proc. 2nd IUTAM Symp. on Structure of Turbulence and Drag Reduction, Zurich, Switzerland.*

CHU, D. C., HENDERSON, R. D. & KARNIADAKIS, G. E. 1992 Parallel spectral element–Fourier simulation of turbulent flow over riblet-mounted surfaces. *Theoret. Comput. Fluid Dyn.* **3**, 219–229.

CHU, D. C. & KARNIADAKIS, G. E. 1991 Numerical investigation of drag reduction in flow over surface with streamwise aligned riblets. *AIAA*-91-0518.

COUSTOLS, E. & COUSTEIX, J. 1989 Experimental investigation of turbulent boundary layers manipulated with internal devices. Riblets. In *Proc. 2nd IUTAM Symp. on Structure of Turbulence and Drag Reduction, Zurich, Switzerland.*

Coustols, E. & Savill, A. M. 1992 Turbulent skin friction drag reduction by active and passive means. *Tech. Rep.* AGARD FDP/VKI. Von Karman Institute, Brussels.

Dean, R. B. 1978 Reynolds number dependence of skin friction and other bulk flow variables in two-dimensional rectangular duct flow. *Trans. ASME* I: *Fluids Engng* **100**, 215–223.

Djenidi, L., Liandrat, J., Anselmet, F. & Fulachier, L. 1986 Viscous effects in drag reduction over riblets. In *Drag Reduction in Fluid Flows: Techniques for Friction Control* (ed. R. H. Sellin & R. T. Moses), pp. 35–41.

Falco, R. E., Klewicki, J. C. & Pan, K. 1989 Production of turbulence in boundary layers and potential for modification in the near wall region. In *Proc. 2nd IUTAM Symp. on Structure of Turbulence and Drag Reduction, Zurich, Switzerland.*

Gaudet, L. 1987 An assessment of the drag reduction properties of riblets and the penalties of off-design conditions. *Royal Aircraft Establishment Tech. Memo*, Aero2113, pp. 363–376.

Gupta, A. K. & Kaplan, R. E. 1972 Statistical characteristics of Reynolds stress in a turbulent boundary layer. *Phys. Fluids* **15**, 981–985.

Hooshmand, A. 1985 An experimental investigation of the influence of a drag reducing longitudinally aligned, triangular riblet surface on the velocity and streamwise vorticity fields of a zero-pressure gradient turbulent boundary layer. PhD thesis, University of Maryland.

Karniadakis, G. E. 1989 Spectral element simulations of laminar and turbulent flows in complex geometries. *Appl. Numer. Maths* **6**, 85–105.

Karniadakis, G. E. 1990 Spectral element–Fourier methods for incompressible turbulent flows. *Comput. Meth. Appl. Mech. Engng* **80**, 367–380.

Karniadakis, G. E., Israeli, M. & Orszag, S. A. 1991 High-order splitting methods for the incompressible Navier–Stokes equations. *J. Comput. Phys.* **97**, 414–443.

Khan, M. S. 1986 A numerical investigation of the drag reduction by riblet surfaces. *AIAA*-86-1127.

Kim, J., Moin, P. & Moser, R. 1987 Turbulence statistics in fully developed channel flow at low 19. *J. Fluid Mech.* **177**, 133–166.

Kline, S. J. & Robinson, S. K. 1989 Turbulent boundary layer structure: Progress, status, and challenges. In *Proc. 2nd IUTAM Symp. on Structure of Turbulence and Drag Reduction, Zurich, Switzerland.*

Kreplin, H. & Eckelmann, H. 1979 Behavior of the three fluctuating velocity components in the wall region of a turbulent channel flow. *Phys. Fluids* **22**, 1233–1239.

Launder, B. E. & Savill, A. M. 1988 Recent developments in the modeling of thin rectangular riblets and manipulators. In *Proc. 3rd Turbulent Drag Reduction Working Party, ONERA-Chantillon, Paris.*

Liu, K. N., Christodoulou, C., Riccius, O. & Joseph, D. D. 1989 Drag reduction in pipes lined with riblets. In *Proc. 2nd IUTAM Symp. on Structure of Turbulence and Drag Reduction, Zurich, Switzerland.*

Luchini, P., Manzo, F. & Pozzi, A. 1991 Resistance of a grooved surface to parallel flow and cross-flow. *J. Fluid Mech.* **228**, 87–109.

Lynch, F. T. & Klinge, M. D. 1991 Some practical aspects of viscous drag reduction concepts. *Proc. Aerospace Tech. Conf., Long Beach, CA*, (*SAE Tech. Paper* 912129).

Moin, P. & Kim, J. 1982 Numerical investigation of turbulent channel flow. *J. Fluid Mech.* **118**, 341–377.

Orszag, S. A. & Patera, A. T. 1983 Secondary instability of wall-bounded shear flows. *J. Fluid Mech.* **128**, 347–385.

Patera, A. T. 1984 A spectral element method for fluid dynamics: laminar flow in a channel expansion. *J. Comput. Phys.* **54**, 468–488.

Robert, J. P. 1992 Drag reduction: an industrial challenge. *Technical report, Airbus Industries, preprint.*

Robinson, S. K. 1988 Effects of riblets on turbulence in a supersonic boundary layer. *AIAA*-88-2526.

Robinson, S. K. 1989 A review of vortex structures and associated coherent motions in turbulent boundary layers. In *Proc. 2nd IUTAM Symp. on Structure of Turbulence and Drag Reduction, Zurich, Switzerland.*

ROON, J. B. & BLACKWELDER, R. F. 1989 The effects of longitudinal roughness elements and local suction upon the turbulent boundary layer. In *Proc. 2nd IUTAM Symp. on Structure of Turbulence and Drag Reduction, Zurich, Switzerland.*

SMITH, C. R. & METZLER, S. P. 1983 The characteristics of low-speed streaks in the near-wall region of a turbulent boundary layer. *J. Fluid Mech.* **129**, 27–54.

SMITH, C. R., WALKER, J. D. A., HAIDARI, A. H. & TAYLOR, B. K. 1989 Hairpin vortices in turbulent boundary layers: the implications for reducing surface drag. In *Proc. 2nd IUTAM Symp. on Structure of Turbulence and Drag Reduction, Zurich, Switzerland.*

SQUIRE, L. C. & SAVILL, A. M. 1986 High-speed riblets. In *Proc. European Meeting on Turbulent Drag Reduction, Lausanne, Switzerland.*

TANI, I. 1988 Drag reduction by riblet viewed as roughness problem. *Proc. Japan Acad.* **64**B, 21–24.

TOMBOULIDES, A. G., ISRAELI, M. & KARNIADAKIS, G. E. 1989 Efficient removal of boundary-divergence errors in time-splitting methods. *J. Sci. Comput.* **4**, 291–308.

TSINOBER, A. 1989 Turbulent drag reduction versus structure of turbulence. In *Proc. 2nd IUTAM Symp. on Structure of Turbulence and Drag Reduction, Zurich, Switzerland.*

VUKOSLAVČEVIĆ, P., WALLACE, J. M. & BALINT, J. L. 1987 On the mechanism of viscous drag reduction using streamwise aligned riblets: a review with new results. In *Turbulent Drag Reduction by Passive Means.*

VUKOSLAVČEVIĆ, P., WALLACE, J. M. & BALINT, J. L. 1991 The velocity and vorticity vector fields of a turbulent boundary layer. Part 1. Simultaneous measurement by hot-wire anemometry. *J. Fluid Mech.* **228**, 25–51.

WALKER, J. D. A., SMITH, C. R., CERRA, A. W. & DOLIGALSKI, T. L. 1987 The impact of a vortex ring on a wall. *J. Fluid Mech.* **181**, 99–140.

WALLACE, J. M. 1982 On the structure of bounded turbulent shear flow: a personal view. In *Developments in Theoretical and Applied Mechanics*, vol. XI, p. 509.

WALLACE, J. M. & BALINT, J. L. 1987 Viscous drag reduction using streamwise aligned riblets: survey and new results. In *Turbulence Management and Relaminarisation* (ed. H. W. Liepmann & R. Narasimha), pp. 133–147.

WALSH, M. J. 1980 Drag characteristics of V-groove and transverse curvature riblets. *Prog. Astronaut. Aeronaut.* **72**, 168.

WALSH, M. J. 1990*a* Effect of detailed surface geometry on riblet drag reduction performance. *J. Aircraft* **27**, 572–573.

WALSH, M. J. 1990*b* In *Viscous Drag Reduction in Boundary Layers* (ed. D. Bushnell & J. Hefner), vol. 123, pp. 204–261.

WALSH, M. J. & ANDERS, J. B. 1989 Riblet/LEBU research at NASA Langley. *Appl. Sci. Res.* **46**, 255–262.

WALSH, M. J. & LINDERMANN, A. M. 1984 Optimization and application of riblets for turbulent drag reduction. *AIAA*-84-0347.

WILLMARTH, W. W. & LU, S. S. 1972 Structure of the Reynolds stress near the wall. *J. Fluid Mech.* **55**, 65–92.

ZORES, R. 1989 Numerische untersuchungen mit einem grobauflosenden simulationsmodell fur die turbulente kanalstromung. *Tech. Rep.* IB 221-89 A 24, Institut fur Theoretische Stromungsmechanik, DLR Göttingen.